ACOUSTOELECTRIC INTERACTIONS IN CADMIUM SULFIDE

E. Adler (M.A.Sc.)

ACOUSTOELECTRIC INTERACTIONS IN CADMIUM SULFIDE

by

Eric L. Adler

A thesis submitted to the Faculty of Graduate Studies and Research in partial fulfilment of the requirements for the degree of Doctor of Philosophy

Electrical Engineering Department
McGill University
Montreal, Canada.

April, 1966

ABSTRACT

This research deals with acoustoelectric interactions in CdS. The first part is devoted to an experimental study of acoustoelectric effects occurring under high field conditions. An acoustic amplifier in which trapping effects are important is described, the decay time for current saturation is measured, and extreme non-uniformities in field distributions are measured and discussed.

In the second part, the effect of acoustoelectric interactions on the electrical impedance of a CdS bar is analysed with the assumption that acoustic damping is dominated by electronic effects. In the presence of a biasing drift field the impedance behaviour is drastically modified and under conditions of acoustic amplification the real part of the impedance becomes negative for some frequencies in the neighbourhood of the mechanical resonances. A linear theory for this effect is presented and the magnitude of the impedance changes are illustrated by calculations for a (1 cm) bar of CdS.

ACKNOWLEDGEMENTS

The author would like to express his thanks to Dr. G.W. Farnell, who supervised this research, for his constant encouragement and guidance. Thanks are due to McGill University and the Electrical Engineering Department for granting the author a leave of absence from teaching duties during the academic year 1963/1964 during which time the bulk of the experimental work was carried out. General support from the National Research Council is acknowledged and in particular for financial assistance during the year's leave of sbsence. Many individuals helped in the course of this work and special thanks go to Mr. J. Foldvari for the construction of special parts, Mr. I. Borissov for his photographic skills, and Messrs. T.C. Lim and A.D. Close for help with the diagrams. Special appreciation is expressed to Miss B. Freeman for an excellent typing job.

TABLE OF CONTENTS

CHAPTER I

INTRODUCTION

Acoustoelectric interactions in Cadmium Sulfide, a piezoelectric, semiconducting and photoconducting material have been exhibited and considered. Acoustic wave amplification[1] occurring in the presence of high drift fields is of primary importance. When large enough fields are applied, the carriers acquire a drift velocity greater than the velocity of sound, the electrons lose energy to the acoustic wave, and travelling wave amplification ensues.

This research was started shortly after Hutson, McFee, and White[1] reported amplification of acoustic waves in CdS. A linear theory of acoustic amplification in piezoelectric semiconductors based on elastic wave propagation studies[3] was put forward by White[2]. Current saturation was observed and attributed to the acoustic amplification by Smith[4], and experimental evidence showing its occurrence with acoustic energy flux growth was supplied by McFee[6]. Gains of less than one-half of the predicted values were achieved by Hickernell and Sakiotis[5], and Blötekjaer and Quate[7].

Trapping dynamics were postulated as a cause for this discrepancy[8], and extension of the theory to include these effects enabled successful interpretation of their experimental results. Current instabilities attributed to acoustic wave amplification were observed with a high field[9], and similar oscillations were reported under conditions of non-uniform illumination[11,12].

The first objective here was the construction of an acoustic amplifier to operate at 100 mc, theoretically close to optimum frequency for CdS. Setting up equipment, developing measuring techniques, and overcoming the difficulties in making ohmic contacts to CdS were the main problems during the early phase of this work. When the acoustic amplifier was completed, observations of performance, current saturation, and acoustic flux generation were made and studied.

By this time the results obtained and the developments reported elsewhere were causing a change in the direction of this work. The steady-state field distributions under saturated conditions revealed large non-uniformities or high field domains interpreted as the result of acoustic energy amplification from the thermal background. Current oscillations were easily obtained at high voltages with either uniform or non-uniform illumination. With uniform low-level illumination the oscillation frequency measured was close to the fundamental mechanical resonance which led to the theory that under acoustic amplification conditions the real part of the electrical impedance of a CdS bar becomes negative near one of the mechanical resonances making the system potentially unstable[14]. Experimental results agree with this.

Chapter II is devoted to a discussion of the manufacture and evaluation of ohmic contacts, the assembly of an acoustic amplifier, and the measurement of acoustic attenuation. Use of the trapping theory to obtain good theory-measurement correlation in amplifier experiments, measurements of the decay time for current saturation, and measurements of non-uniform field distributions are presented and discussed in Chapter III. Both types of current instabilities are investigated in Chapter IV. For the oscillations resulting from uniform illumination a linear theory is developed for the electrical impedance of a biased CdS bar, which predicts a negative resistance instability substantiated by experimental results. For the type of oscillation obtained with non-uniform illumination, the frequency of oscillation is found to be dependent on conductivity, voltage and circuit impedance suggesting a high field instability.

CHAPTER II

EXPERIMENTAL TECHNIQUES AND SAMPLE PREPARATION

2.1 Introduction

In measuring the acoustoelectric properties of Cadmium Sulfide both acoustic and electrical measurements were made. The acoustic attenuation was measured by propagating acoustic pulses at ultrasonic frequencies in rectangular bars of CdS by driving a quartz transducer bonded to one end of the bar with a pulsed R.F. oscillator. An identical transducer bonded to the other end of the bar was connected to a sensitive receiver to amplify the pulse which was then displayed. In the acoustic amplifier experiments quartz buffer rods were inserted between each transducer and the Cadmium Sulfide, as shown in Figure 2.1, to provide electrical isolation and time delay[1]. In amplifier experiments the electric field was calculated by dividing the voltage by the sample length. This imposes very stringent requirements on the electrical contacts made to the CdS bars; the making and evaluation of ohmic contacts constituted a difficult technological problem.

In this section the details of attenuation measurement, acoustic amplifier construction, and ohmic contact formation and evaluation will be discussed in detail.

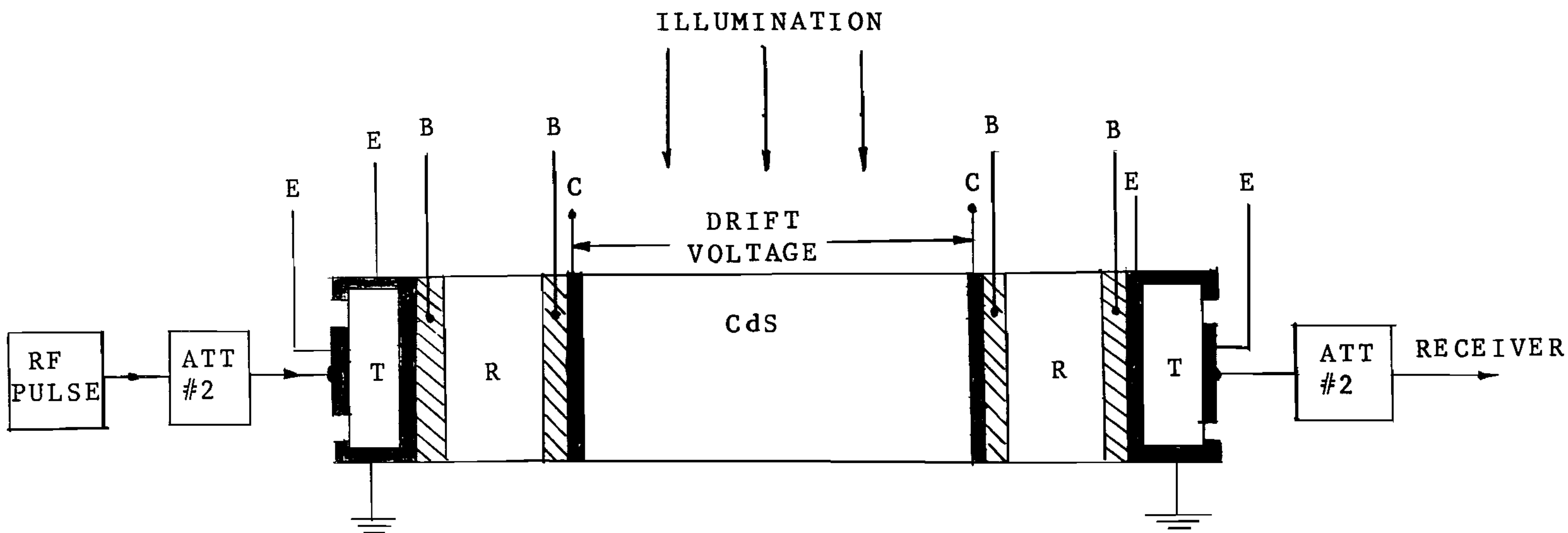

R - BUFFER ROD

B - ACOUSTIC BONDS

T - PIEZOELECTRIC TRANSDUCERS

C - CONTACTS TO SAMPLE

E - ELECTRODES TO TRANSDUCERS

FIGURE 2.1 ULTRASONIC ASSEMBLY

2.2 Acoustic Attenuation Measurement

The change in acoustic attenuation caused by varying the specimen photoconductivity or dc electric field was measured using the assembly shown in Figure 2.1. The two calibrated attenuators were always adjusted to keep the receiver level constant to eliminate errors due to receiver nonlinearity. The change in attenuation was given by the change in total attenuator setting.

Attenuation measurements were made using AC-cut quartz transducers for shear waves and X-cut quartz for longitudinal waves. As the acoustic amplifiers were all shear wave amplifiers[1], the transducers were adjusted for polarization parallel to the hexagonal axis, and the dc field was applied parallel to the propagation direction. Measurements of the amplifier attenuation as a function of drift voltage and conductivity for different frequencies were carried out using the dark transmission level as the reference. The results will be discussed in Chapter III. To avoid heating due to the high fields used, low duty cycle pulses were used for the R.F. drive and drift field necessitating the electronic circuitry shown in Figure 2.2. With this system the drift pulse was adjusted to coincide with the transit of an acoustic pulse in the CdS bar.

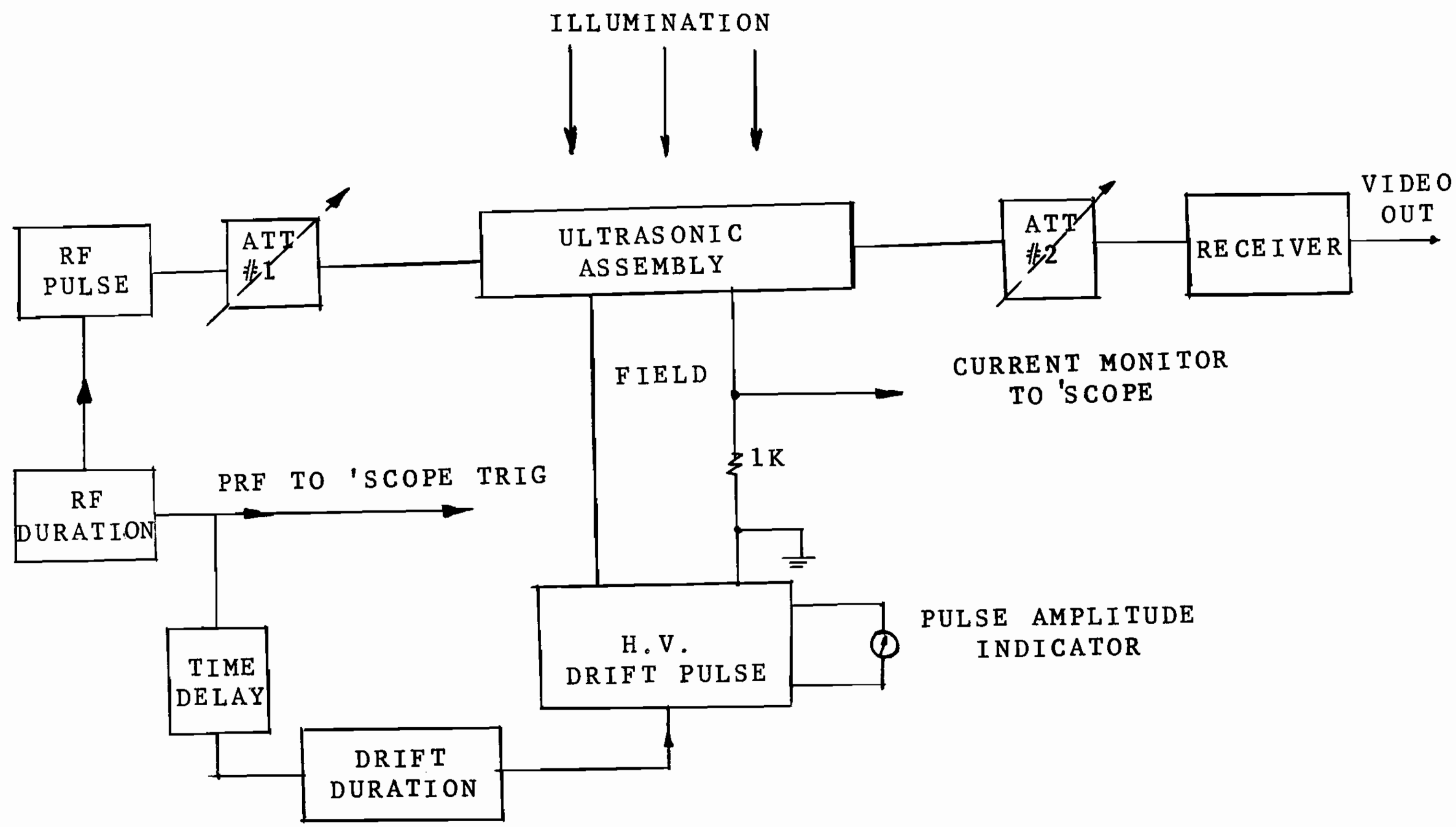

FIGURE 2.2 ELECTRONIC CIRCUITRY

2.3 Acoustic Bonds, Transducers, and Buffers

The buffer rods, one inch long and 1/8 inch diameter providing a time delay of 6.75 μs for shear waves and 4.25 μs for longitudinal waves, were of fused quartz as that has a very low acoustic loss at V.H.F.[10] and is routinely available with the required optical quality end-face parallelism and flatness.

Quartz transducers of 5mc fundamental resonant frequency were driven at high odd harmonics up to about 145mc. The transducers were 1/8 inch diameter plates, specially finished for overtone operation, with a coaxial electrode system.

The acoustic bonds had to have enough shear stiffness at the operating frequencies so that the transmission loss would not be excessive. Many resins[10], epoxies[5], and metallic compression bonds of indium[15] were considered. In the assemblies of Figure 2.1 the bonds were as follows: buffer to CdS, Canada Balsam[20]; and transducer to buffer, Dow Chemical Resin #276-V9[10]. These materials were chosen since bonds made with them are easily assembled and dismantled. At room temperature Canada Balsam is solid and the Dow Resin is very viscous.

Canada Balsam bonds were made by heating the Balsam to about 70°C. and placing a small amount of the softened Balsam on the surfaces to be bonded. When the two previously heated surfaces were pressed together, the still soft excess Balsam

was squeezed out, the bond was allowed to solidify by cooling and the excess Balsam scraped off. To make bonds which were of roughly the same thickness the above assembly was placed in a brass cylinder with a piston mechanism and heated to 100°C. at a piston pressure of about 6 kg/cm^2. The procedure produced a strong bond, thin enough to give a reasonable amount of shear coupling at 100mc. Choice of temperature and pressure was made on the basis of tests described below.
A similar procedure was followed in making bonds with Dow Resin, but since the resin is already soft at room temperature, the preheating phase was bypassed.

To evaluate these bonds an experimental assembly was built consisting of two transducers bonded to a buffer rod. A simple insertion loss measurement for the many different temperatures and pressures was taken to be a measure of the bond transmission loss. The lowest insertion loss was obtained with Balsam bonds assembled at 100°C. and 6 kg/cm^2 and with Dow Resin bonds at 100°C and 3 kg/cm^2.

The acoustic amplifiers were assembled using these by making the two Canada Balsam bonds for the "CdS-buffer rod sandwich" and allowing this to harden. The two transducer bonds were then made and after cooling this constituted the complete structure shown in Figure 2.1.

2.4 Ohmic Contacts

Ohmic contacts were made to the semiconductor bars to ensure a known uniform field, calculable from the applied voltage and sample length. Contacts were considered to be ohmic when they had the following properties:

a) Non-rectification of current,

b) Negligible voltage drop at the contacts, and

c) Linear current voltage characteristic at low voltages.

These requirements are by no means trivial and achieving them with high resistivity CdS was quite a difficult problem. Attempts to purchase samples with ohmic contacts were very disappointing as tests showed them to be either rectifying or nonlinear.

Experimenting with indium contacts and developing methods for evaluating the results required much detailed work. This work was started on a trial and error basis; eventually developing into the systematic procedures described below. Since the equipment available for these studies made it necessary to work with one sample at a time, a prolonged period was spent on this phase of the research. The contacts were made by diffusing indium into the CdS to a depth large enough to overcome surface effects and make contact to the bulk material. Initially, this was done by evaporating a layer of indium over the regions of the bar where contacts were needed, and heating the bar in an inert atmosphere at about 400°C. for approximately 5 minutes, and allowing the crystal to cool quite slowly. Great care was taken at each phase to avoid contaminating the crystal. Since this did not always give satisfactory contacts, heat treatment studies were carried out as described in Section 2.4.2.

2.4.1 Evaluation of Contacts

After a contact was made, the current-voltage characteristic was displayed on an oscilloscope, ac. voltage amplitude of about 20V., revealing any rectification or nonlinearity present. If this characteristic was linear, the photoconductance was measured as a function of bar illumination. If this was linear[21] at low light intensities when the free electron density is a small fraction of the trap density, it was interpreted as a verification that the contacts were ohmic since bulk photoconductive properties were being measured. Even if both of these tests were satisfactory, there was still the possibility of a high contact resistance, and profile measurements were made to verify that the field in the specimen was uniform and determined by the applied voltage and the sample length.

The profile measurements were made with a bronze wire as a potential probe connected to an oscilloscope 10MΩ probe by placing the wire tip on the CdS surface and forming a temporary non-rectifying contact using a tesla discharge. The results shown in Figure 2.3 exhibited substantial scatter and, therefore, were only a qualitative indication of the presence of high voltage drops near the contacts. Curve A, sample EP1#3, shows there was a uniform field over most of the crystal length, somewhat less than V/L, and near one end a short high field region attributed to the contact at the end. Curve B, sample Har#2, shows a uniform field, equal to V/L, over the entire length, and the contacts were considered to be ohmic. At the time of making these measurements both samples had a linear current-voltage characteristic and at low illumination a linear photoresponse characteristic.

One more measurement, the current-voltage characteristic at high voltages, was made to observe the acoustoelectric phenomenon of current saturation. The existence of saturation, the voltage at which this occurred, and the hardness of the saturation were all indications of the quality of the crystal and contacts.

2.4.2 Heat Treatment Studies

A series of heat treatment studies were made on some crystals to optimize the making of contacts and to relate their quality with the results of the different evaluation procedures. The studies consisted of heating the CdS samples in a hydrogen atmosphere for 30 minutes at 250°C., allowing the samples

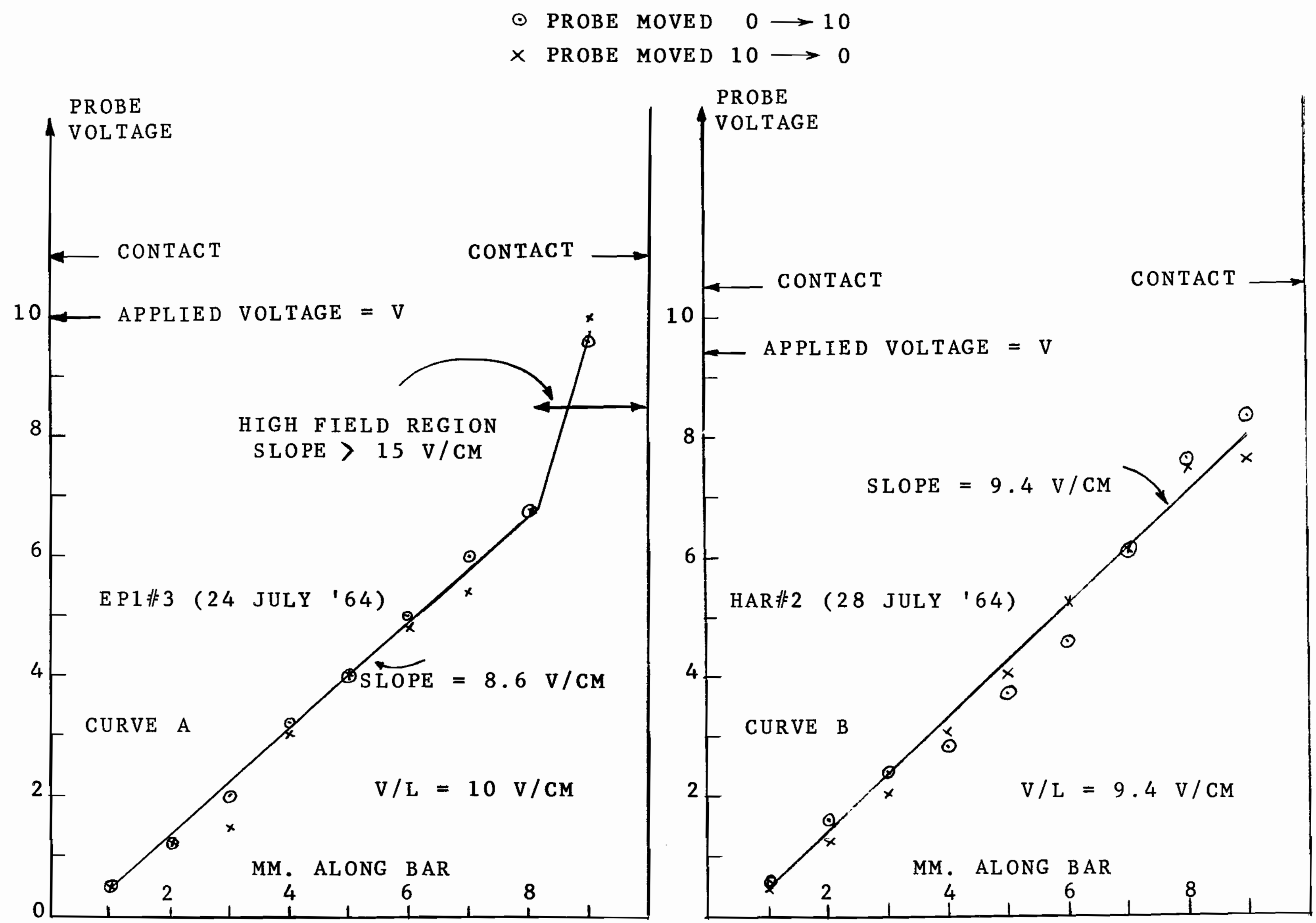

FIGURE 2.3 POTENTIAL PROFILES

to cool, and measuring:

1) Linearity of current-voltage characteristic,
2) Photoconductive response, and
3) Current saturation characteristic.

This cycle was repeated with some convenient increases in time and temperature. A reducing atmosphere was used in the heat runs to avoid surface oxidation problems which have been reported[22].

The results obtained for sample Har#2 are shown in Figure 2.4 and Figure 2.5. A table of the heat treatment sequence is shown, Table 2.1, with four of the photoresponse curves, Figure 2.4. The current-voltage characteristics of all four were linear but for curve #1 and #2 of Figure 2.4 this linearity could only be approximately achieved by forming the contacts with a tesla discharge. In Figure 2.5 the saturation characteristics are plotted for four stages of the heat treatment; the labelling of these curves is the same as Figure 2.4. These measurements were made using 40 μs voltage pulses at 30 pulses per second allowing the current to saturate fully before the end of the pulse and keeping the power dissipation low. The effects of heat treatment sequences are summarized here:

1) The slope of the log-log photoconductance plots approaches unity at low illumination.

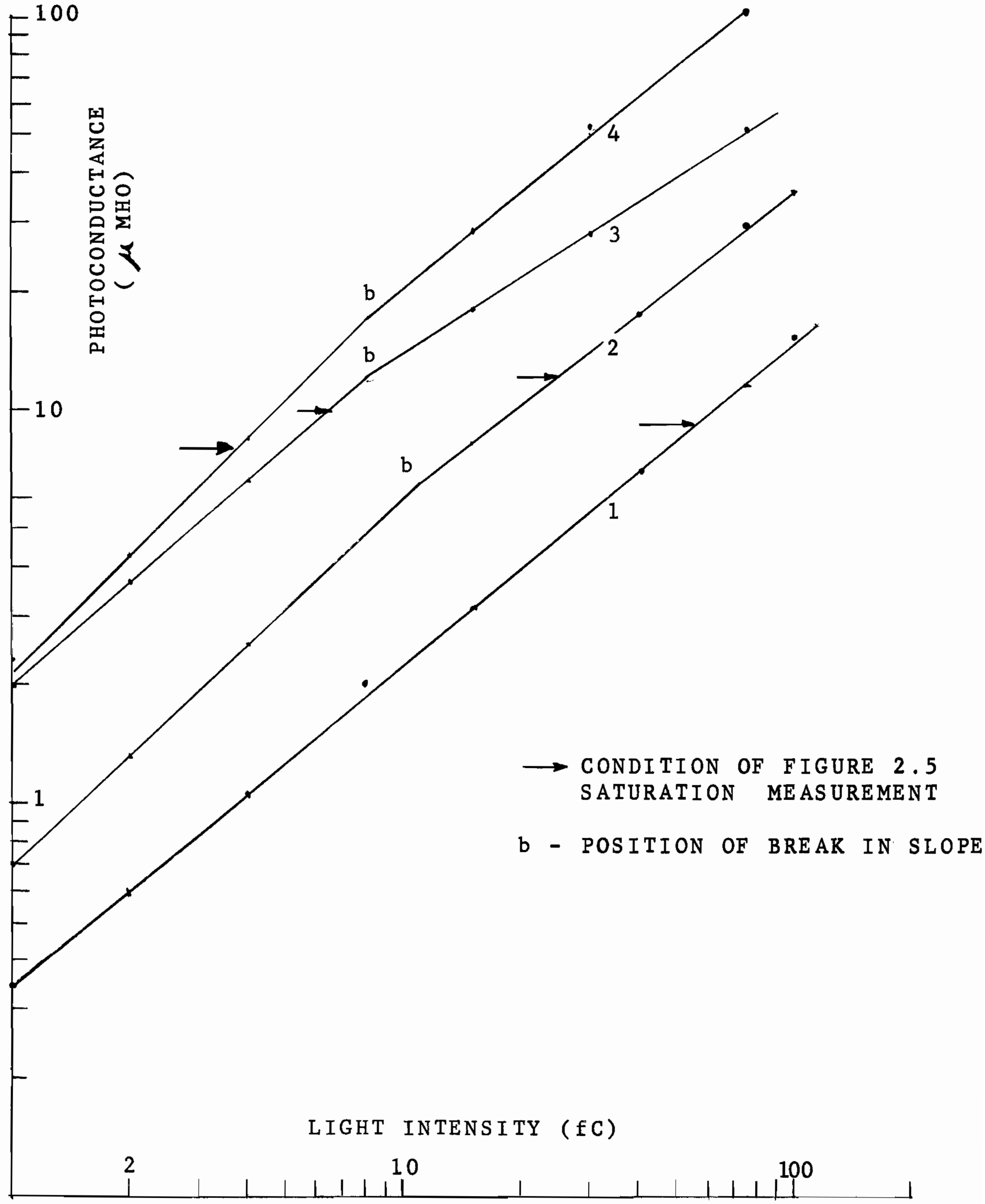

FIGURE 2.4 PHOTOCONDUCTANCE RESPONSE FOR SAMPLE HAR#2

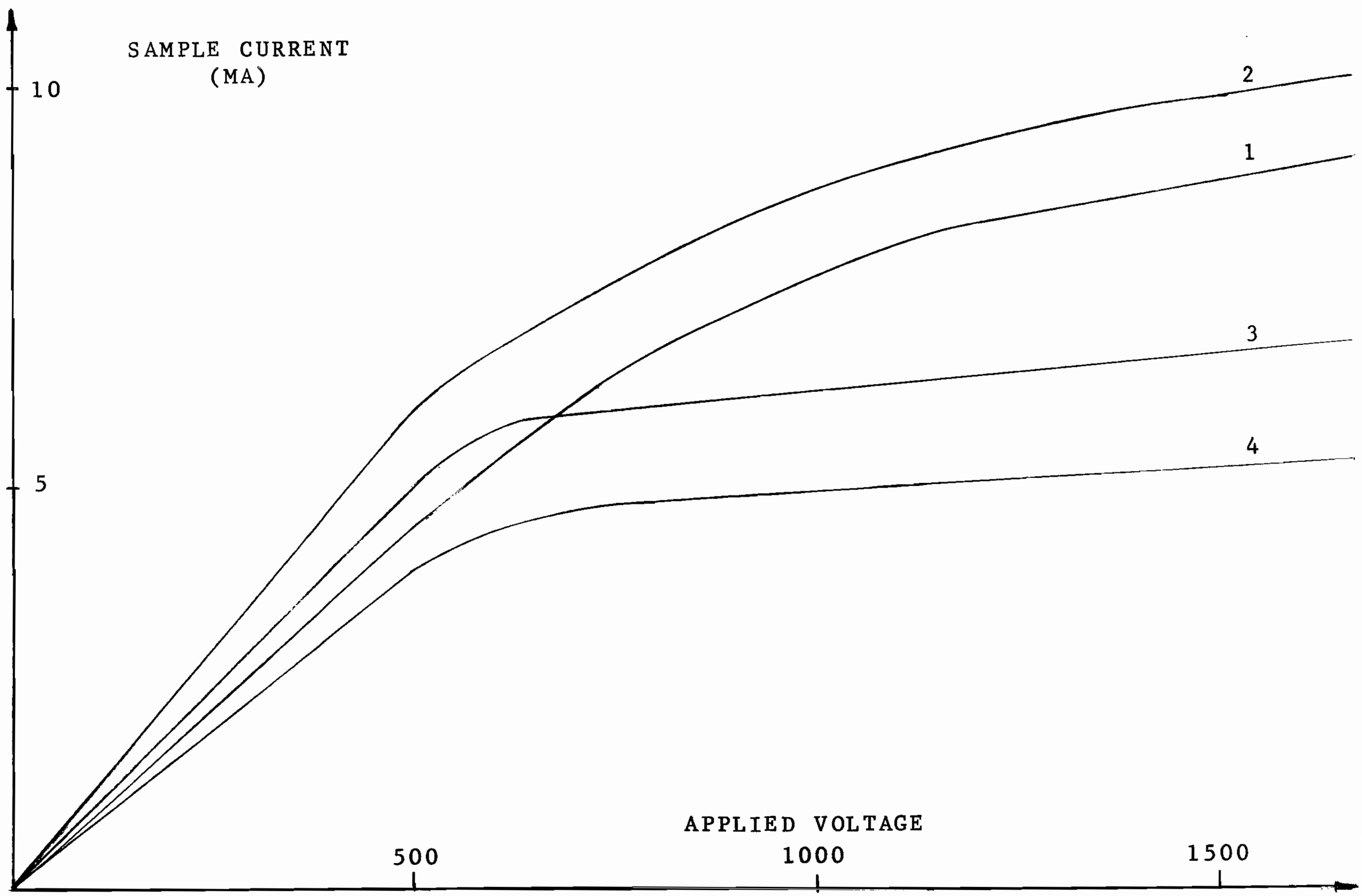

FIGURE 2.5 SATURATION CHARACTERISTICS FOR SAMPLE HAR#2

TABLE 2.1

	Heating Treatment Data			Low Illumination Properties From Fig. 2.4			Saturation Properties From Fig. 2.5	
Curve	Time Mins	Temp °C.	Date	Log-Log Slope	Sensitivity μmho/F.C.	% Change in Adjacent	Saturation Voltage	Ratio of Slopes Ohmic/Sat.
1	30	250	20/7/64	.78	.25	-	850	6:1
2	60	250	20/7/64	.92	.33	30%	720	6:1
N.S.	30	300	21/7/64	.93	1.0	300%	630	10:1
3	60	300	21/7/64	.86	1.6	60%	575	12:1
N.S.	90	300	22/7/64	.88	1.5	6%	575	9:1
4	5	400	23/7/64	.98	2.1	40%	575	15:1
N.S.	30	300	24/7/64	1.0	2.3	10%	575	15:1

SUMMARY OF DATA FROM FIGURE 2.4 AND FIGURE 2.5

N.S. Not Shown in Figure 2.4 or Figure 2.5

2) The photosensitivity (in μmho/fc, defined as dG/dF) improvement becomes negligible, levelling at about 2 μmho/fc. (Note: Although for any <u>one</u> curve of Figure 2.4 the light meter and illumination source positions were kept constant, comparisons of the illumination in fc <u>between</u> any curves cannot be made to better than about $\pm 20\%$).

3) The saturation voltage, calculated by finding the intersection between a linear extrapolation of the ohmic and the high field regions of Figure 2.5, decreases towards a constant value of 575 volts.

4) The hardness of saturation, as measured by the ratio of the ohmic to non-ohmic slopes of the current-voltage characteristic, approaches a constant value of about 15:1.

2.4.3 <u>Conclusion</u>

At the conclusion of the heat treatment sequence the contacts are ohmic. Assuming the changes observed are dominated by contact effects, the four items listed above are taken as evidence for this statement, since the photoconductance and the current-voltage characteristic each tend to a definite limit implying that no further significant changes in the contacts was occurring. Contact effects must be negligible because linearity of the photoconductance-illumination characteristic is a bulk property, and this is what was measured. The potential profile measurement which was previously discussed, curve B in Figure 2.3, was obtained from this sample at the conclusion of these heat run tests and serves to confirm the field uniformity which results from the ohmic contacts.

The electron drift mobility was estimated to be 300 $cm^2/v.sec.$ from the saturation voltage in Figure 2.5 and the shear wave velocity. The trap density was estimated as $5 \times 10^{12}/cc$ from the conductivity value at which the slope breaks for curve #4 in Figure 2.4 indicating a very pure crystal[21].

In summary, procedures for evaluating contacts were developed based on the measurement of a linear current-voltage characteristic, a linear conductance-illumination characteristic, a linear surface potential distribution and a sharp saturation of current at a well defined voltage. When these conditions are all satisfied, a good ohmic contact has been made. Making ohmic contacts and testing them is an important problem in acoustoelectric investigations and other techniques are currently being investigated as an extension of the work described above.

CHAPTER III

ACOUSTOELECTRIC PHENOMENA - STEADY STATE

In CdS, a piezoelectric photoconducting semiconductor, a large number of effects arising out of electron-lattice interactions have been observed. The important steady state phenomena discussed in this section are:

1) Photosensitive attenuation of acoustic waves.
2) Amplification of acoustic waves.
3) High voltage current saturation.
4) Acoustic flux generation at high voltage.
5) Non-uniform field distributions at high voltages.

3.1 Photosensitive Acoustic Attenuation

3.1.1 Introduction

The report[18] that acoustic attenuation in CdS was sensitive to illumination for certain polarizations of the ultrasonic wave led Hutson and White[3] to develop a linear theory for this effect based on the interaction of the photoelectrons with the piezoelectric fields accompanying the acoustic wave. Since CdS is hexagonal, this interaction exists for acoustic waves polarized parallel to the hexagonal axis. If trapping is neglected, the acoustic attenuation due only to this interaction is

$$\alpha = (K^2/2)\ (\omega_c/v_S)/\left[1 + \left(\frac{\omega_c}{\omega} + \frac{\omega}{\omega_D}\right)^2\right] \qquad (3.1)$$

Using the notation of Hutson and White[3] in which

K is the electromechanical coupling constant appropriate to the wave propagation direction and polarization.

$\omega_c = \sigma/\epsilon$, the dielectric relaxation frequency.

$\omega_D = v_S{}^2/D_n$, the diffusion frequency.

v_S is the velocity of sound in cm/sec.

D_n is the diffusion constant for electrons.

σ is the conductivity.

Attempts at verification of equation (3.1) have been only semiquantitative due to illumination anomalies[19] and geometric uncertainties resulting from irregularly shaped samples[23]. In the experiment described below, the theoretical predictions of equation (3.1) were verified by measuring the change in attenuation in CdS as a function of conductivity.

3.1.2 Experimental Arrangement and Results

The attenuation of shear waves polarized parallel to the hexagonal axis was measured for different values of illumination at an ultrasonic frequency of 75 mc using the circuit of Figure 2.2 and the assembly shown in Figure 2.1. The specimen conductance, simultaneously measured, was controlled by varying the incandescent illumination. This measurement was made for two signal levels; one very weak in which the attenuation of the first transmitted pulse was measured, the other much stronger in which the attenuation of the first echo due to reflections in the quartz was measured.

3.1.3 Interpretation of Results

At a frequency of 75 mc and the highest conductivity used, ω_c/ω is less than or equal to 0.05 and ω/ω_D is equal to 0.10, therefore $\omega_c \ll \omega \ll \omega_D$. Under these conditions the attenuation will be independent of frequency in equation (3.1) and is

$$\alpha = (K^2/2)\ (\omega_c/v_s)\ \text{Np/cm}\ ; \qquad (3.2)$$

a linear relationship between α and σ. When trapping effects are taken into account in the attenuation calculation, equation (3.2) is still valid.

The total attenuation of a specimen having length L cm, cross-section A cm^2, and conductance $G = \sigma A/L$ mho is

$$\alpha L = (K^2/2)\ (GL^2/\epsilon v_S A)(8.68)\,db \quad . \qquad (3.3)$$

For the specimen tested: $L = 1$ cm, $A = 9 \times 10^{-2}$ cm^2,

$$\sigma = 11\ G\ \text{mho/cm},$$

$$\epsilon = 80 \times 10^{-14}\ \text{F/cm},$$

$$v_S = 1.75 \times 10^5\ \text{cm/sec.},$$

$$K^2/2 = 0.018.$$

Equation (3.3) predicts an attenuation-conductance slope

$$\alpha L/_G = (K^2/2)\ (L^2/\epsilon v_S A)\ (8.68)$$

$$= 12 db/\mu mho\ .$$

As seen in Figure 3.1 the measured results show excellent quantitative agreement with this prediction. Using longitudinal transducers and propagating in the same direction, no change in attenuation was detected as the photoconductance

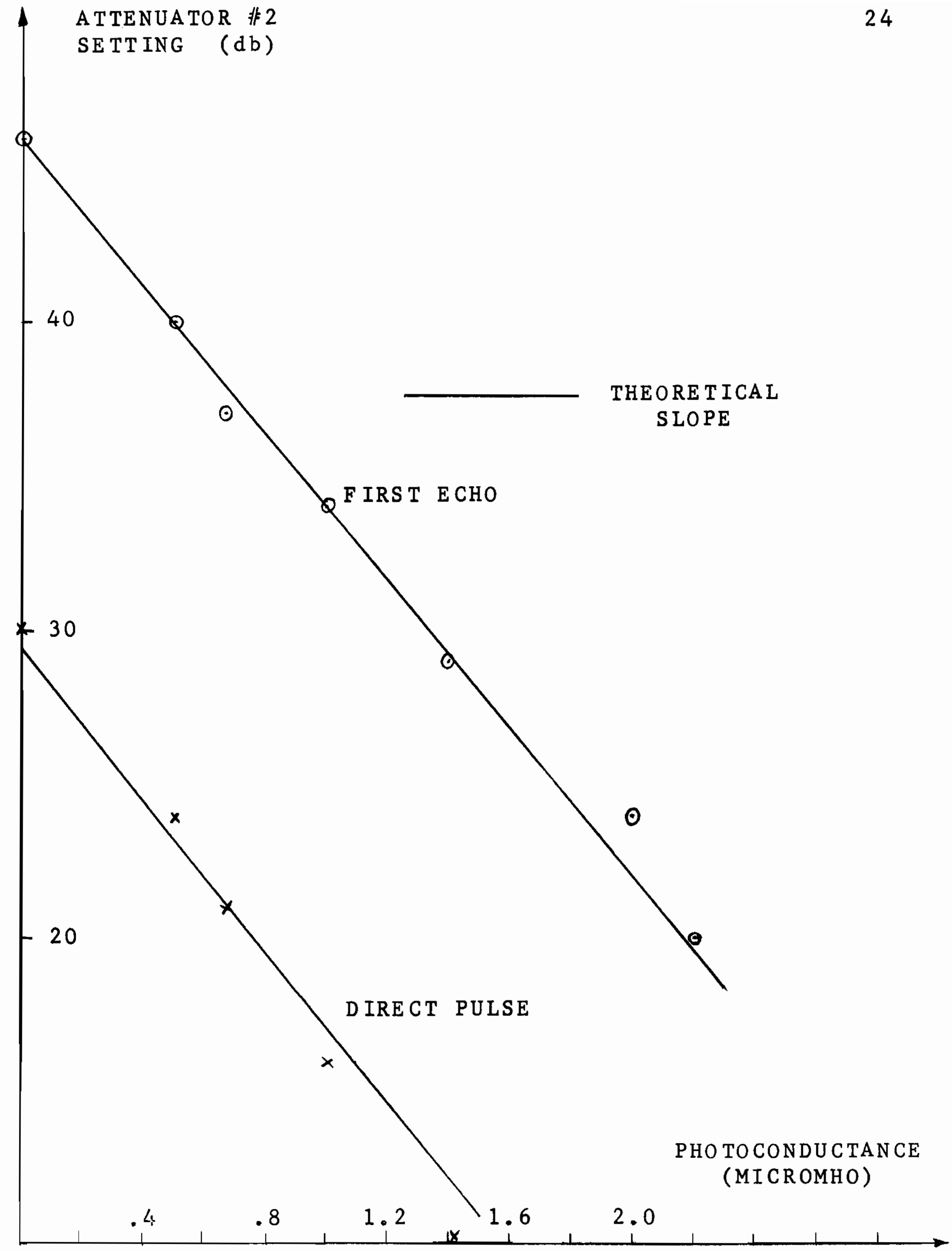

FIGURE 3.1 75 MC ATTENUATION OF SHEAR WAVES IN CdS
FOR SAMPLE EP1#2

was changed. Since this particular wave does not couple to the carriers, this result agrees with the theory.

3.2 Acoustic Amplification

3.2.1 Introduction

In the presence of a D.C. electric field the carriers in CdS will acquire a drift velocity parallel to the field causing the acoustic wave attenuation to differ from the zero field case. When the carriers are moving in synchronism with the wave, there is no interaction, and the acoustic loss due to the carriers vanishes; but when the drift velocity exceeds the sound velocity, the carriers will bunch and energy will transfer from the electron system to the acoustic wave yielding travelling-wave amplification of the acoustic wave. White's linear theory[2], neglecting the dynamics of carrier trapping, shows acoustic attenuation as

$$\alpha = \frac{\dfrac{K^2\omega_c}{2\ v_S}\left(1 - \dfrac{f_o v_D}{v_S}\right)}{\left(1 - \dfrac{f_o\ v_D}{v_S}\right)^2 + \left(\dfrac{\omega_c}{\omega} + \dfrac{\omega}{\omega_D}\right)^2} \qquad (3.5)$$

where v_D is the electron drift velocity, and f_o is the fraction of the space charge in the conduction band. When the carrier drift velocity equals the velocity of sound and there is no trapping, $f_o = 1$, α will change sign.

Acoustic amplifier experiments[1,7,8] show a fair qualitative agreement, but quantitatively the gain is one-half to one-third the predicted values. Carrier trapping dynamic effects can account for most of the discrepancies. Uchida et al[8] assume a characteristic trapping time, τ, in addition to f_o, the equilibrium fraction of acoustically produced mobile space charge. This makes the fraction, f, of space charge, mobile under dynamic conditions, a complex function of frequency:

$$f = (f_o - i\,\omega\tau) / (1 - i\,\omega\tau) \,. \qquad (3.6)$$

Two real parameters, a and b, are defined by

$$f = b\, f_o / (1 + i\, a) \qquad (3.7)$$

which makes

$$a = (1 - f_o)\,\omega\tau / (f_o + (\omega\tau)^2) \qquad (3.8)$$

and

$$b\, f_o = (f_o^{\,2} + (\omega\tau)^2) / (f_o + (\omega\tau)^2) \,. \qquad (3.9)$$

If $f_o = 1$, then a = 0 and b = 1 for all frequencies, corresponding to no trapping effects. Gain can now be written in terms of a and b

$$\alpha = (K^2 \omega_c / 2v_S) \frac{(1 - bf_o v_D/v_S) + a(a + \omega b f_o/\omega_D)}{(1 - bf_o v_D/v_S - a\,\omega_c/\omega)^2 + (a + \omega_c/\omega + \omega b f_o/\omega_D)^2}$$

(3.10)

Here $bf_o v_D$ defines an effective drift velocity, and a occurring in the numerator causes a greater acoustic loss than in equation (3.5).

3.2.2 Amplifier Response Measurements

The gain characteristic of an acoustic amplifier was measured as detailed in Section 2.2 on an assembly utilizing crystal EP1#2. The results obtained at a photoconductivity of 28 KΩcm and frequencies of 75 and 95 mc are shown in Figures 3.2 and 3.3.

3.2.3 Discussion of Results

For this amplifier from equation (3.5) a predicted maximum gain of about 120 db over the entire 60 - 120 mc frequency band should be possible, but the results obtained are frequency sensitive and show only about one-third that gain.

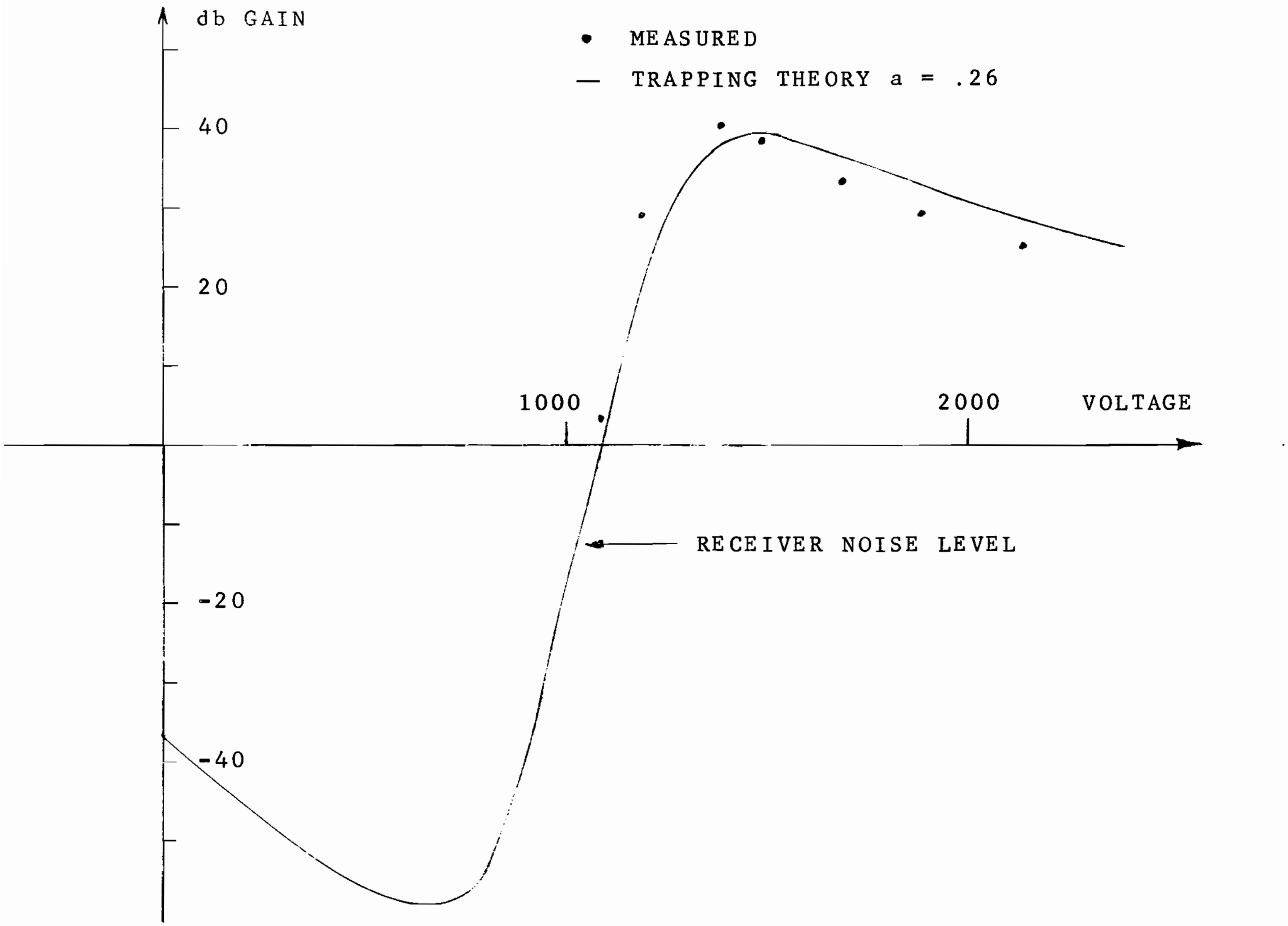

FIGURE 3.2 GAIN CHARACTERISTIC OF CdS AMPLIFIER AT 95 MC
AND SAMPLE RESISTANCE 300 KΩ

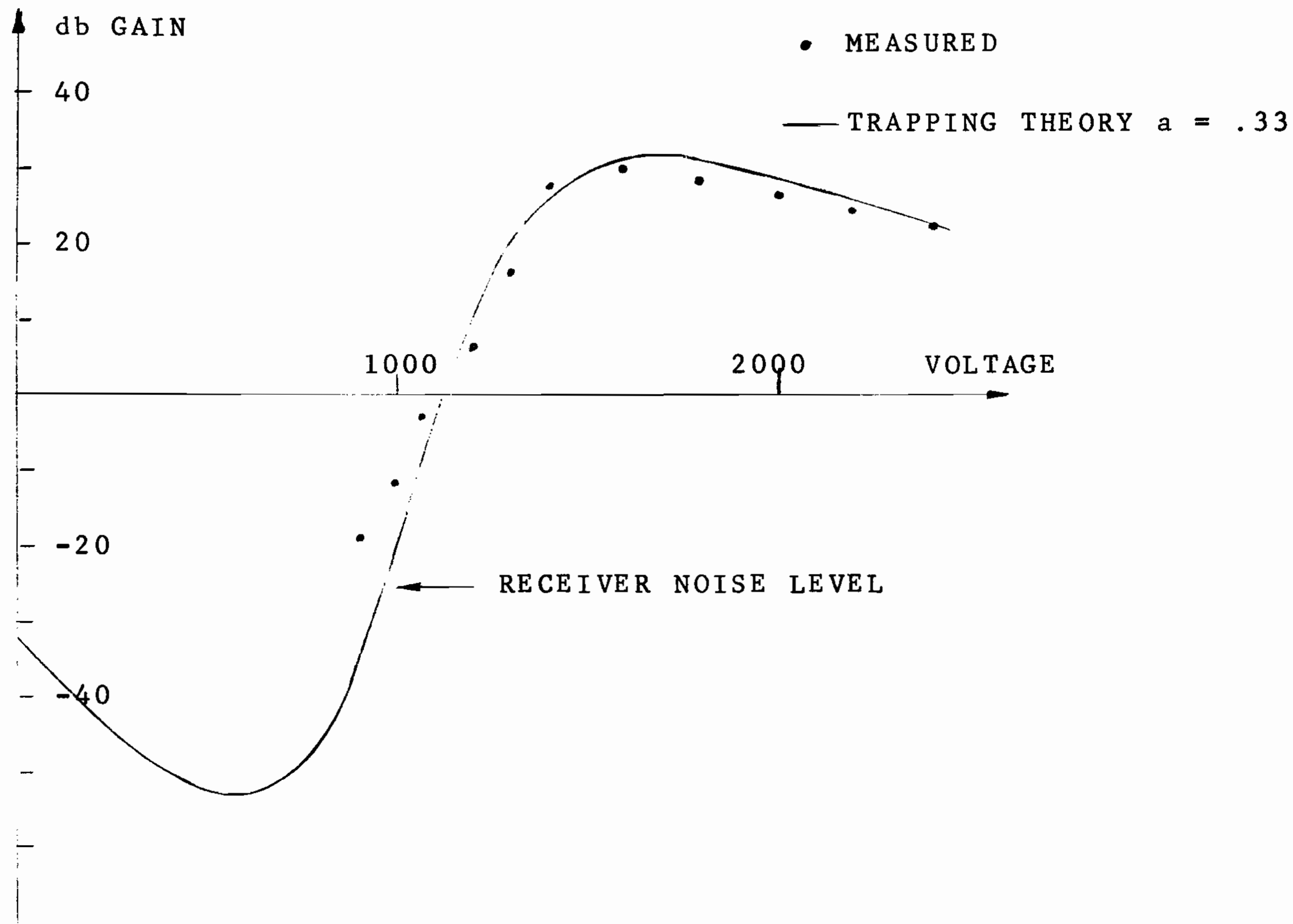

FIGURE 3.3 GAIN CHARACTERISTIC OF CdS AMPLIFIER
AT 75 MC AND SAMPLE RESISTANCE 300 KΩ

Interpreting this as an indication that trapping effects are important for this sample at these frequencies, equation (3.10) was plotted in the solid curves in Figures 3.2 and 3.3. The best fit occurred with $bf_o = 1$, $\omega\tau > f_o$, and $a = 0.33$ at 75 mc or $a = 0.26$ at 95 mc. The ratio of these two values for a is equal to the inverse ratio of the frequencies, as would be expected, since $\omega\tau > f_o$ implies $a = (1 - f_o)/\omega\tau$ from equation (3.8). From equations (3.8) and (3.9) and the values of a found above it can be seen that the characteristic trapping time, τ, lies between 4.3 and 6.5 nanoseconds. In addition to accounting for the deviations from the simple theory, the Uchida theory supplies a possible tool for measuring characteristic trapping times and cross sections in piezoelectric semiconductors[24]. At present there is a lack of independent knowledge about the parameters involved, and there is a need to investigate trapping by some independent means to establish the validity of this theory.

White[25] has just reported successfully growing sulfur doped crystals having a large enough trapping time that amplifier performances are in good agreement with the simple theory above 50 mc.

3.3 Current Saturation and Acoustic Flux Generation

3.3.1 Introduction

Under conditions of acoustic gain the current through a CdS bar saturates sometime after the application of the dc voltage. This phenomenon was reported by Smith[4] for both photoconducting and semiconducting CdS. He proposed that the mechanism of acoustic amplification comes into effect generating a growing acoustic wave large enough to trap the carriers so that they are unable to drift faster than the velocity of sound. Smith was unable to detect such acoustic waves.

McFee[6] observed similar saturation in his amplifier experiments and correlated this current saturation with the build up of acoustic flux in the CdS samples. The flux was detected by the output transducers whenever the drift pulses were longer than 100 μs.

At this time Hutson[26] explained this non-ohmic behaviour as the result of the dc acoustoelectric current accompanying the acoustic flux generated by travelling-wave amplification. He postulated that a steady-state value for the flux will be reached when the amplitude of the flux is large enough to cause nonlinear loss by pairwise interference of amplified waves to produce a third wave at a sum frequency where there is net loss of acoustic energy. The equal-frequency mixing also generates a dc acoustoelectric current which subtracts from the ohmic current.

McFee[6] lends some support to this theory by delaying the input signal pulse to an acoustic amplifier so that amplification occurs in the presence of flux. He finds a decrease in gain in the presence of flux and infers that the signal is losing energy by entering into non-linear mixing with the flux according to Hutson's theory. Almost all acoustic amplifiers to date have been operated on a pulsed basis where the signal amplification takes place before any significant acoustic flux builds up.

In the measurements described below most of the preceding results are verified and some new experimental results having a strong bearing on the mechanism of saturation and flux generation are discussed.

3.3.2 Experiment and Results

Without applying any input, the output from the amplifier and the current through the CdS were simultaneously monitored using the circuit in Figure 2.2. Photographs #1, 2, 3 and 6 of Figure 3.4 display the flux growth and the current saturation at practically the same time, after allowing a 7 μs delay for the flux in the buffer rod. Since the flux

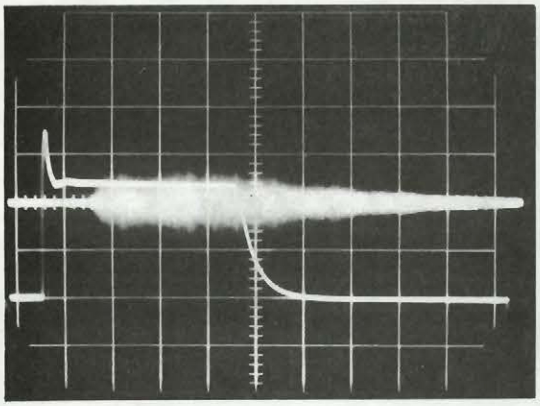

1. CURRENT SCALE, 5 MA/CM; HORIZONTAL SCALE, 10μS/CM.

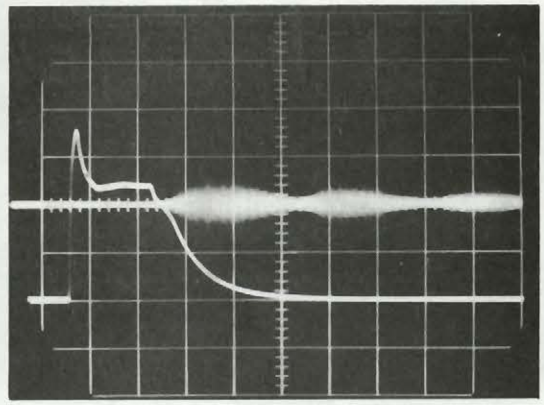

2. CURRENT SCALE, 5 MA/CM; HORIZONTAL SCALE, 5μS/CM.

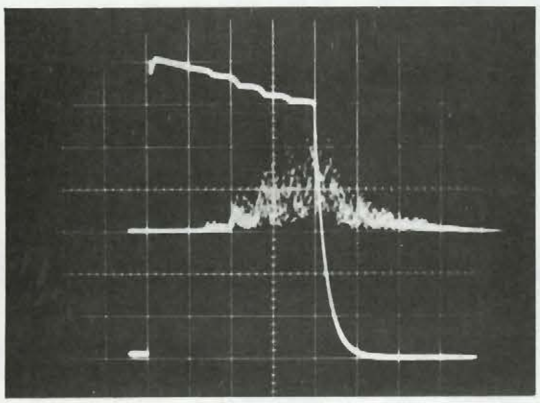

3. CURRENT SCALE, 1 MA/CM; HORIZONTAL SCALE, 20μS/CM.

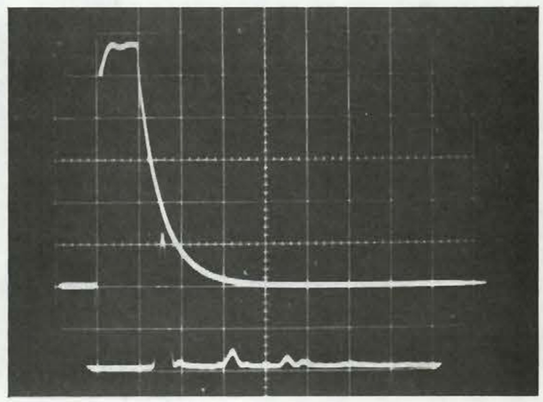

4. CURRENT SCALE, 1 MA/CM; HORIZONTAL SCALE, 10μS/CM.

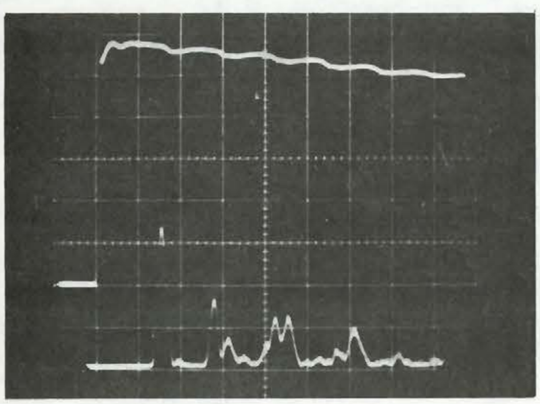

5. SCALES AS IN 4.

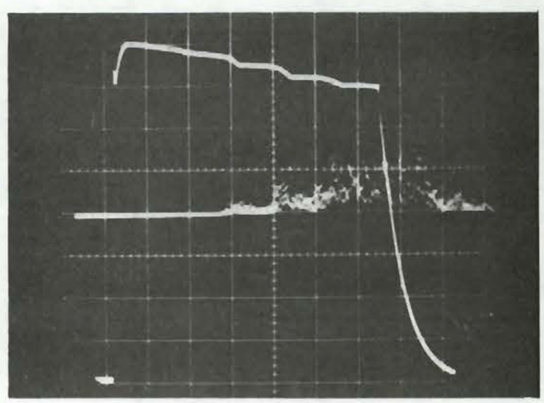

6. SCALES AS IN 4.

FIGURE 3.4 CURRENT SATURATION AND ACOUSTOELECTRIC FLUX. DRIFT VOLTAGE 1500V. PHOTOS 1 AND 2, SAMPLE EP1#3; PHOTOS 3, 4, 5, AND 6, SAMPLE EP1#2 was observed at frequencies 10 mc apart from 50 to 150 mc, the tuning range of the receiver, its acoustic origin must be very broadband. This property and the fact that the flux occurs with the current saturation agrees with the theory[26] and results[6]. Figure 3.5 depicts typical saturation characteristics.

Measuring the time taken for the current to saturate as a function of conductivity at different applied voltages in many samples, it was found that the time depends almost exponentially on the sample resistivity if the time exceeds one acoustic round-trip and almost linearly otherwise. In either case saturation time increased with resistivity and voltage as can be seen in Figures 3.6 and 3.7.

Similar measurements have been reported[28] in which the saturation time was found to increase with resistivity but decrease with voltage. These measurements were made for resistivities less than 10^{-4} Ωcm which corresponds to the region in Figure 3.7 for which the resistance is less than 0.1M Ω. In this region, if the results are extrapolated to lower resistivities, a change in the voltage dependence would be obtained in agreement with these reports.

3.3.3 Interpretation of Results

The results for sample EP1#3 at a conductance of approximately 20 μmho illustrates the concurrent build up

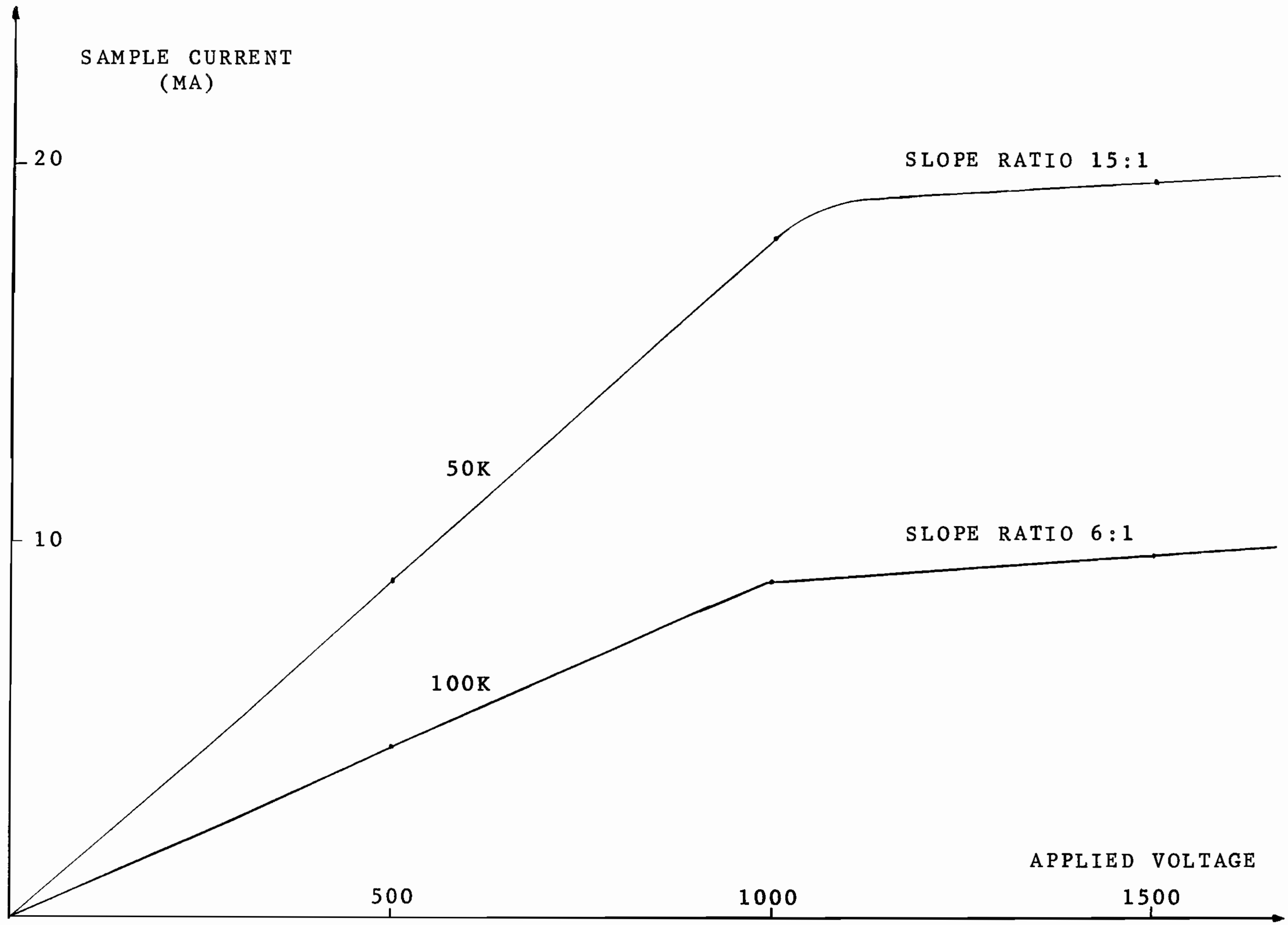

FIGURE 3.5 CURRENT SATURATION CHARACTERISTIC FOR SAMPLE EP1#3

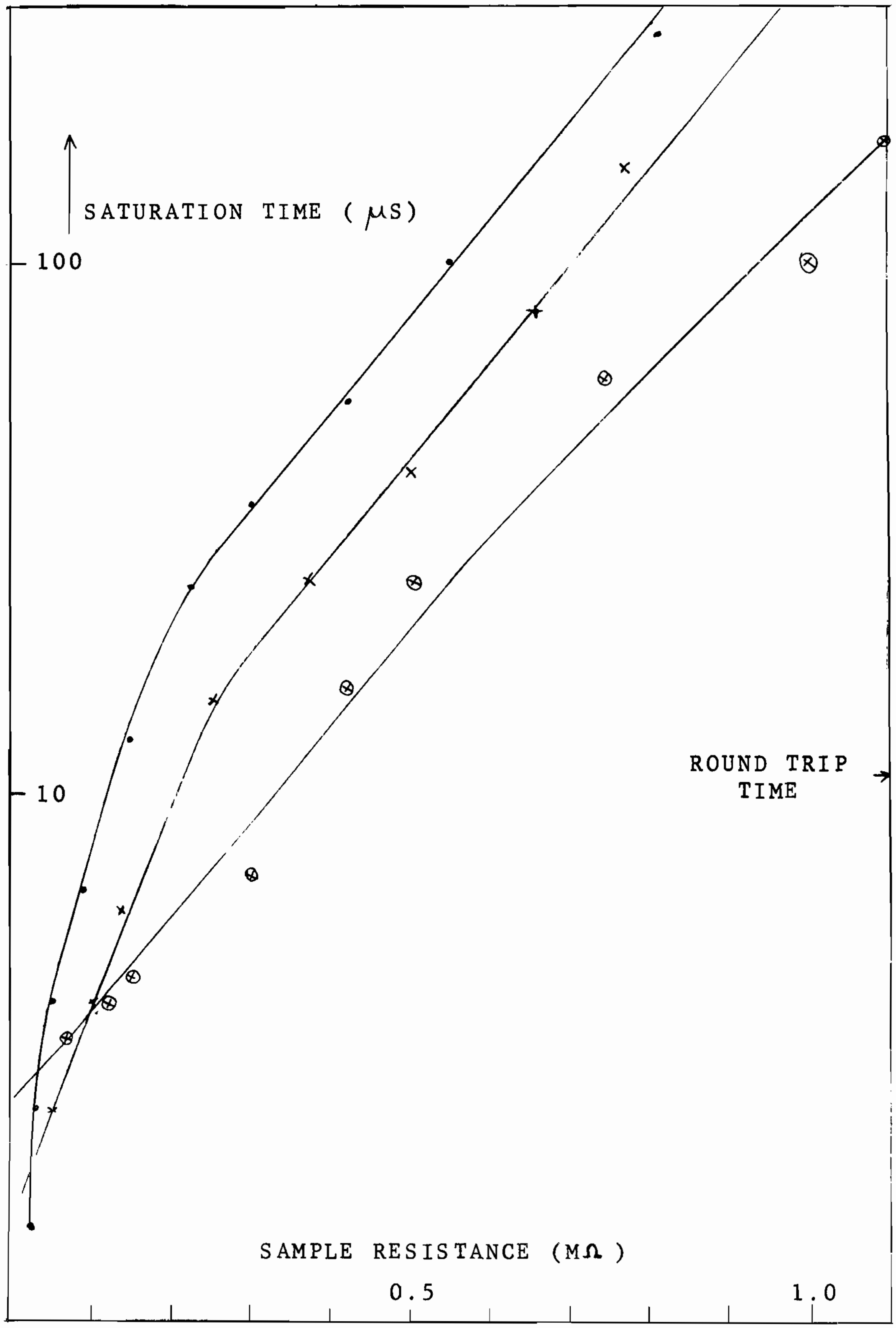

FIGURE 3.6 ONSET OF SATURATION FOR SAMPLE HAR#2

TABLE

VOLTS	MEASURE SLOPE	CALC SLOPE	RATIO
1500	85μS/MΩ	6.5	13
1000	36 "	3.0	12
750	14 "	1.22	11.5

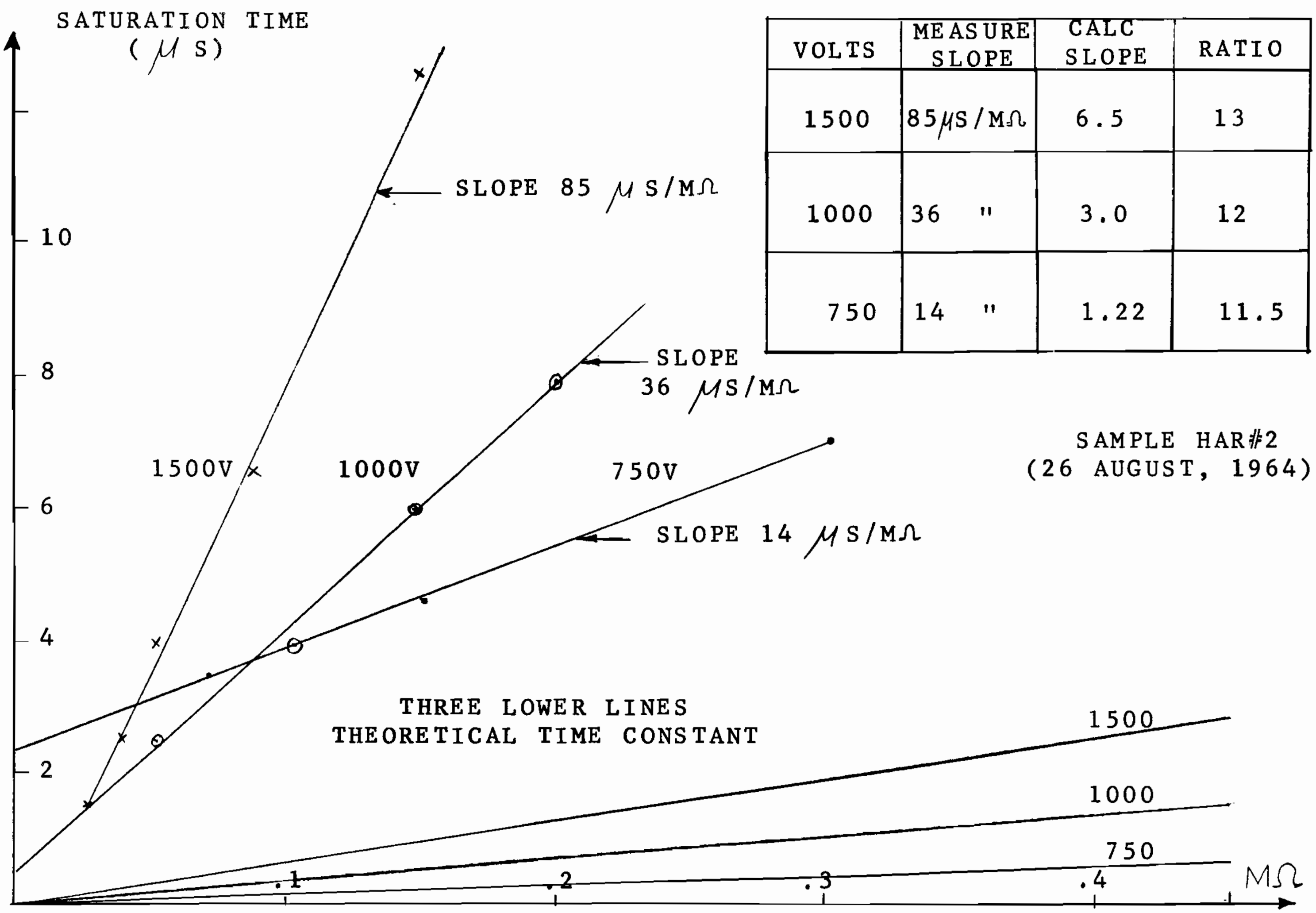

SAMPLE HAR#2
(26 AUGUST, 1964)

FIGURE 3.7 SATURATION TIME FOR DIFFERENT SAMPLE RESISTANCES of acoustic flux and current saturation in an amplifier. The acoustic flux after being delayed for 7 μs in the output buffer rod is seen in Photo #1, Figure 3.4, as a noise waveform starting about 10 μs after the drift current plus starts and 7 μs after it saturates. Allowing for the buffer rod propagation delay means that the flux build up occurs at the same time as the current saturates. The drift voltage pulse was shortened considerably, and in Photo #2 a flux pulse can be seen to echo in the output buffer rod. In both instances the flux build up and the current saturation occur in 3 μs, about half a transit time in the CdS bar. The simultaneous occurrence of these two effects concurs with McFee's experimental results and constitutes evidence supporting Hutson's explanation.

The results at lower conductivities are rather different and can be seen for measurements made on sample EP1#2. The conductance is 5 μmho in Photo #3, Figure 3.4, and the acoustic flux is seen to build up over many transits. The current waveform is decaying in a series of acousto-electric ripples due to the reflection of acoustic flux between the sample end faces. With a high voltage there is net acoustic gain in one round trip, and as a pulse propagates from cathode to anode, it is amplified causing a greater decrease in the external current when the pulse is near the anode. The period of those ripples is equal to the round trip transit time, 11.5 μs. This acoustoelectric current decrease can be produced by an injected sound pulse. In Photos #4 and #5 the lower trace shows the amplified acoustic pulses after transmission through the amplifier assembly; the upper trace shows the current pulse with a visible acoustoelectric dip. The pulse is on just long enough to amplify the acoustic pulse in Photo #4, whereas in Photo #5 a very long pulse is used showing amplification and interaction of echoes with the flux.

The input sound is removed and the receiver gain increased to reveal the flux in Photo #6. The current waveform is now clear of the acoustoelectric dips which were caused by the input sound wave. As the flux builds up, the current can be seen to decay almost stepwise with step duration essentially equal to one acoustic round trip. At the time of making these measurements the pulse generator could not supply a very wide pulse so that the final current saturation cannot be seen.

The amplification of acoustic energy from the thermal background proceeds until it is limited in the steady-state by non-linear mixing which produces an acoustoelectric current and causes the current taken by the crystal to decrease. Figure 3.8 displays this process in block form. The dynamics of the flux growth will be determined by non-linear mechanisms for which there is no complete theory at present.

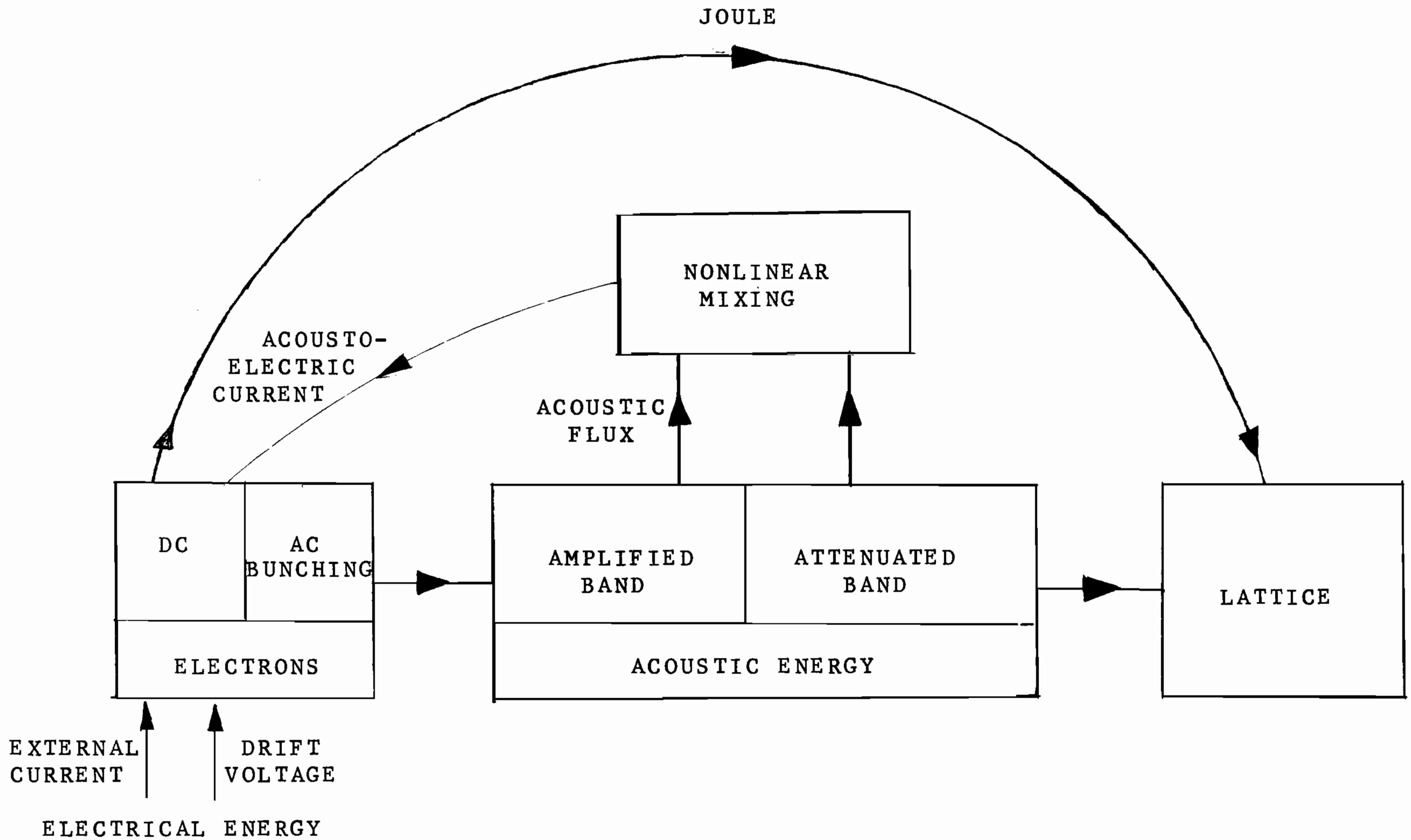

FIGURE 3.8 NONLINEAR PROCESSES IN AMPLIFYING CdS

The time constant determining the decay of an acoustic wave is $\tau = 1/\alpha v_S$ where α is calculated from equation (3.5). As this will be negative under gain conditions, a wave will grow with time, and under conditions of moderately high field, the time constant for frequencies $\omega_c < \omega < \omega_D$ will be approximately

$$\tau = (2/_{K}2)\ (1 - \mu E/v_S)\ /\ \omega_c \qquad (3.11)$$

This time constant increases with field and resistance concurring with the measured results shown in Figure 3.7. The time constant was calculated from equation (3.11) and the comparison with measured results tabulated in Figure 3.7 indicates that it takes 12 time constants for saturation to take place. This value represents amplification of the thermal background by 12 nepers, 104 db or 160,000.
Let us assume for an order of magnitude calculation that thermal background is Johnson noise, corresponding to an RMS noise field

$$\overline{E_n} = (4kTRB)^{\frac{1}{2}}\ /\ L \qquad (3.12)$$

which is linearly amplified up to the dc field value V/L.

If $R = 10^5\ \Omega$, $B = 10^9$ c/s (an upper limit on the amplified waves)[27], and $V = 1000$ volts the ratio of these two fields

$$E_{DC} / \overline{E_n} = \frac{1000}{\sqrt{4 \times 1.4 \times 10^{-23} \times 300 \times 10^5 \times 10^9}} = 770{,}000$$

This is within order of magnitude agreement and all which could be expected in view of the simplified model used.

Figures 3.5 and 3.6 indicate that an extrapolation of the linear theory is not possible for a saturation time of many acoustic round trips, as the reflection losses and formation of non-uniformities in the electric field will dominate the dynamics of flux growth and current saturation.

3.3.4 Secondary Pulses

Secondary pulses trailing the directly amplified shear pulse have been observed[29] and interpreted as a collective wave propagation of momentum. With one of the amplifiers assembled here a somewhat similar secondary pulse, trailing the main pulse by about 3 μs, was observed but could be attributed to longitudinal $\longrightarrow$ shear mode conversion on reflection at the input buffer to CdS interface.

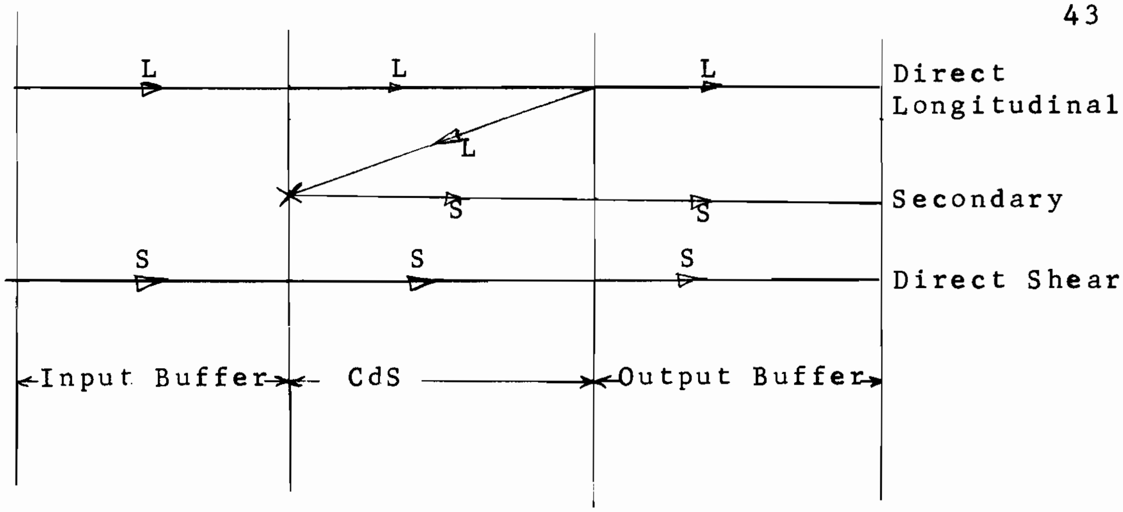

× Conversion Interface

In support of the mode conversion interpretation, the following is stated:

1) If the drift pulse was terminated before conversion could occur, no secondary pulse was observed.
2) Using longitudinal transducers when the amplifier was under gain conditions, a pulse was obtained at the same time location as the secondary pulse.
3) If the amplifier was turned around, the secondary pulse was always observed, even with a short drift pulse; consistent with conversion occurring only at the one interface marked on the diagram.

The mode conversion is attributed to either a wedge shaped bond or non-parallelism of the end faces. Since both propagate with the same velocity in the output buffer, changing only this length would not make any difference in the time interval between the main and secondary pulses.

3.4 Nonuniform Field Distributions at High Voltages

3.4.1 Introduction

When a crystal is in an amplifying state, the growth of acoustic flux generates a dc acoustoelectric current. As noted above, the current saturation has been attributed to this acoustoelectric current subtracting from the ohmic current. The acoustoelectric current will be large in regions where the flux amplitudes are large and since the net current in a bar must be constant along its length, there will be a corresponding increase in the conduction current. Neglecting any significant carrier accumulation effects, the conduction current can only increase by an increase in the electric field. As the flux amplitudes will be highest near the anode terminal of a crystal, the electric fields are expected to be highest there. Since a constant voltage is applied in amplifier and saturation experiments, if the field near the anode grows, the field near the cathode must decay. Potential probe measurements of the electric field reveal substantial non-uniformities in qualitative agreement with these predictions.

3.4.2 Experimental Procedure and Results

In addition to contacts at the two ends indium strip contacts were made along one surface of sample Har#2. To do this, a brass shimstock mask was made having ten 0.01 inch slots spaced 0.025 inches apart. Indium was evaporated onto the masked sample, and the sample was heated to diffuse the indium into the CdS. Potential profile measurements were made under conditions of uniform illumination. The sample resistance was about 100 KΩ corresponding to a resistivity of 10 KΩ cm.

To measure the potential profile, a brass probe, which could be raised and lowered by a screw adjustment, was mounted on a micrometer driven carriage. The probe tip, connected to an oscilloscope, was positioned to touch the contact strips by viewing through a microscope. Voltage pulses, 40 μs duration and 30 pps, were applied to the sample. Within 30 μs the current was fully saturated, and the potential distribution was then measured for applied voltages above and below current saturation.

The potential profile results obtained from one polarity and five different values of applied voltage are shown in

Figure 3.9. The field distributions were calculated from these profiles and are plotted in Figure 3.10. These results show vividly that the field distributions become grossly non-uniform when the applied voltage exceeds the saturation value; the high field building up at the anode end of the bar.

It can be seen from Figure 3.10 that there are some non-uniformities inherent in the crystal. In Curve I the low-voltage field distribution exhibits a slightly higher value near the anode end. Since the illumination was quite uniform, this was probably due to an intrinsic non-uniformity in conductivity. The current waveform was found to exhibit damped oscillations for a few cycles after application of the voltage pulse before attaining a steady state value.

A drastic change in the high field distribution at high voltages occurs when the polarity of the applied voltage is reversed. The potential profile results are shown in Figure 3.11; the field distributions are calculated and plotted in Figure 3.12. A high field region now exists near the center of the bar and the field even changes sign near the anode. The low-voltage field distribution is not measurably changed, but at high voltages current saturation is much quicker and shows no sign of damped oscillations.

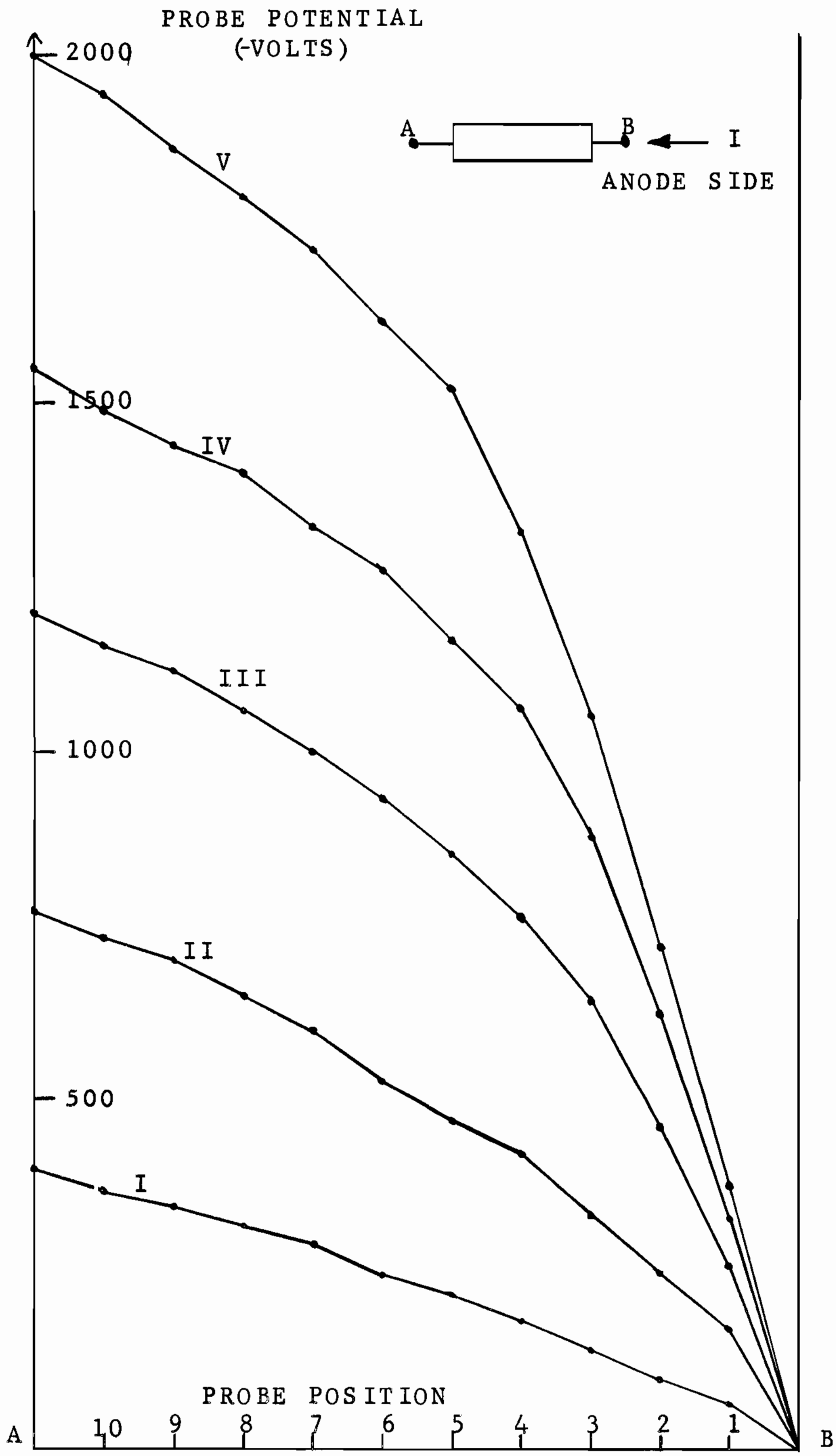

FIGURE 3.9 POTENTIAL PROFILES FOR SAMPLE HAR#2 (28 JULY, 1965). RESISTANCE = 100 KΩ.

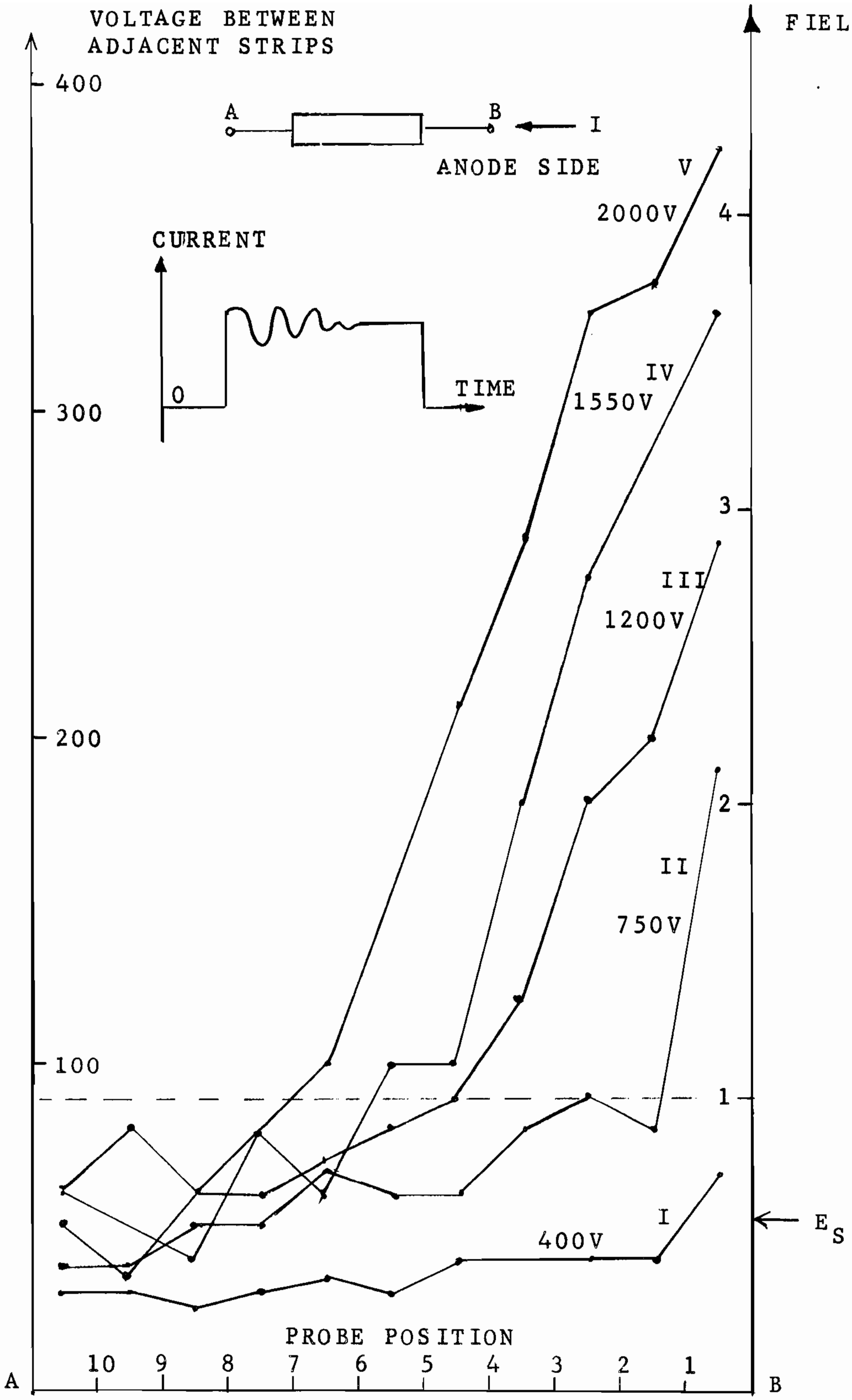

FIGURE 3.10 CALCULATED FIELD DISTRIBUTION CORRESPONDING TO FIGURE 3.9

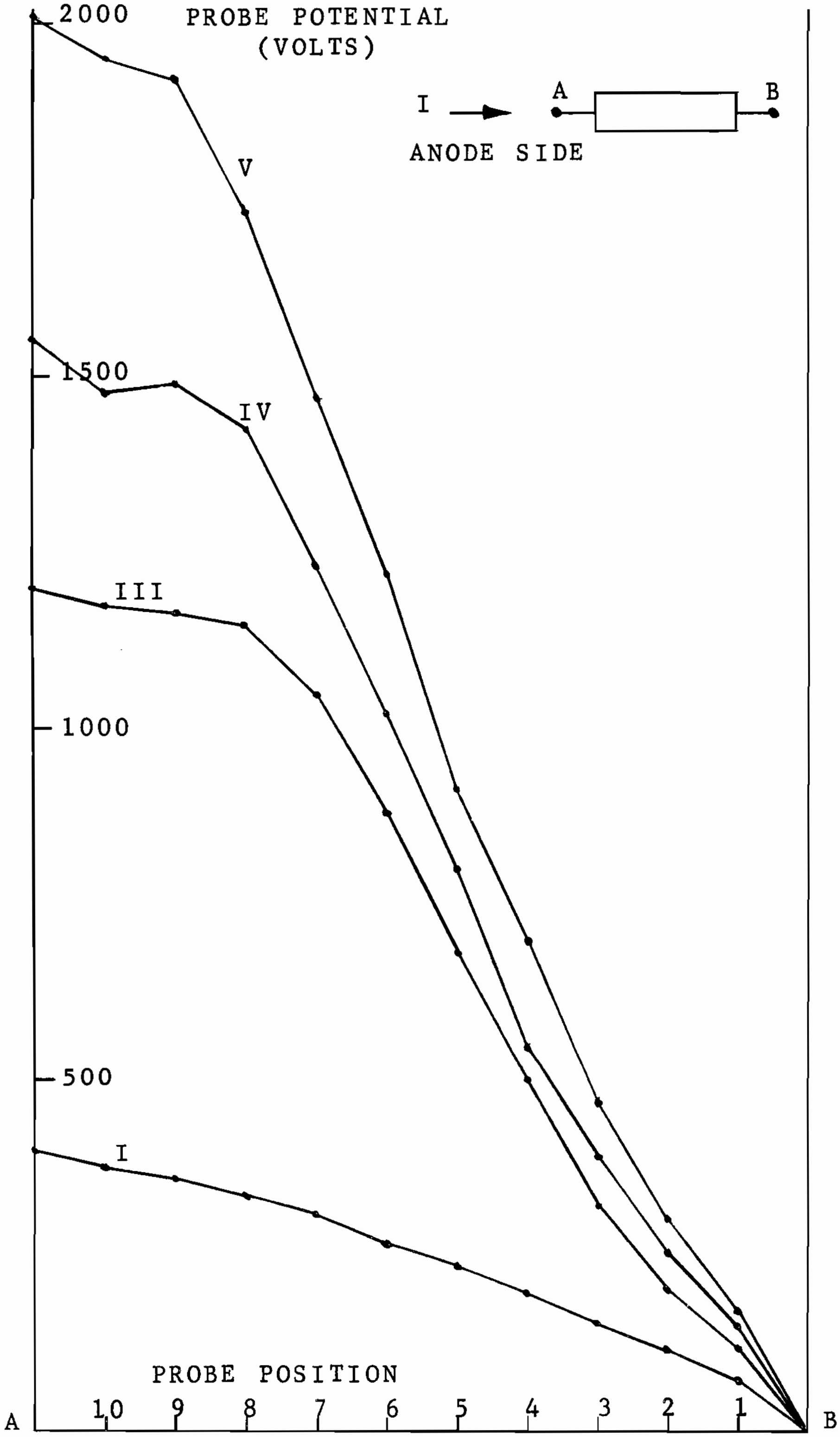

FIGURE 3.11 POTENTIAL PROFILES
FOR SAMPLE Har#2

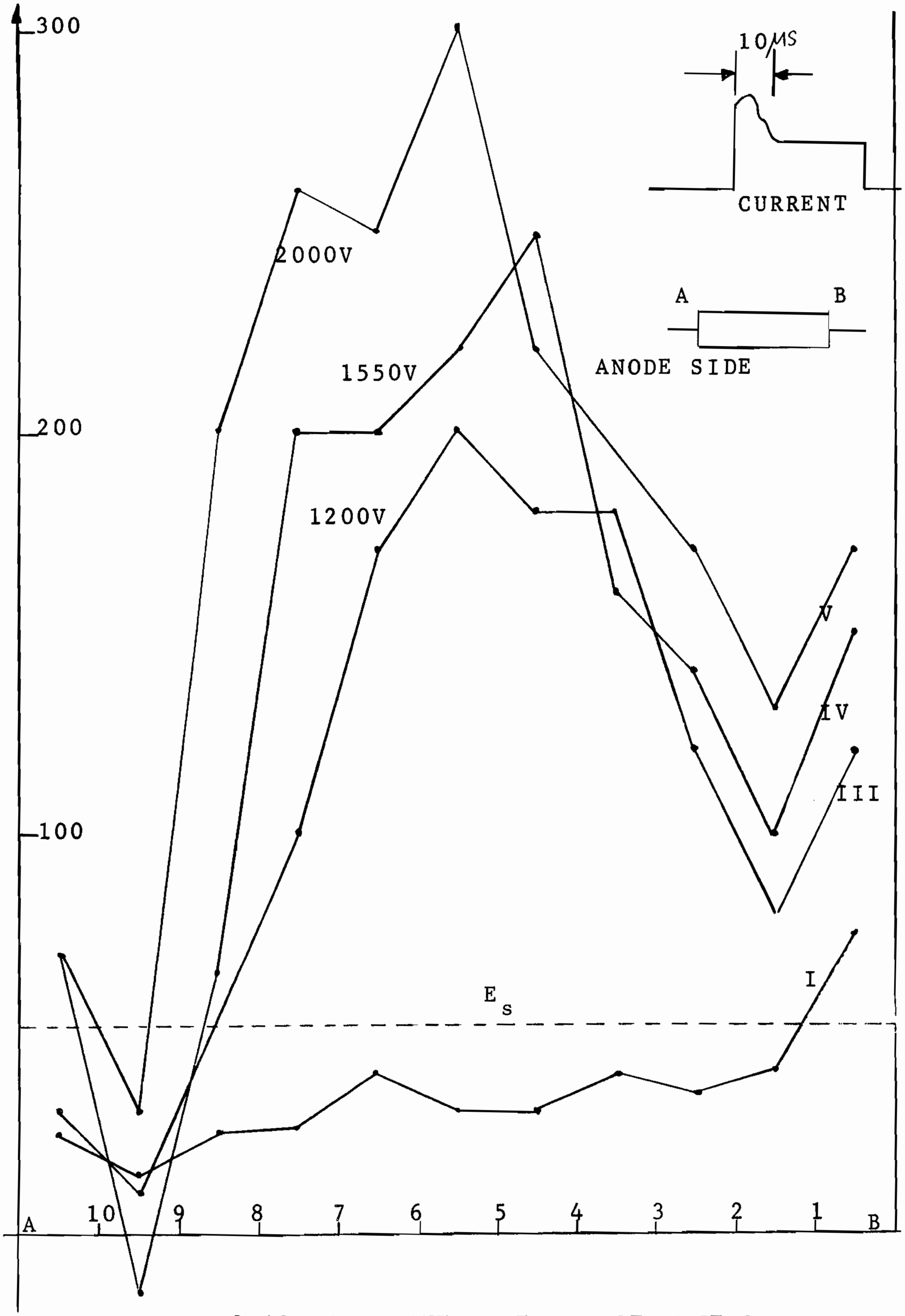

FIGURE 3.12 CALCULATED FIELD DISTRIBUTION CORRESPONDING TO FIGURE 3.11

3.4.3 Discussion of Results

The results shown in Figure 3.10 are in qualitative agreement with the expectations that high-field regions would be built up under conditions of amplification in the regions near the anode. To calculate the local acousto-electric currents from these distributions and get some information on the steady state amplifying properties of the crystal, we need to know the acoustoelectric current in terms of the measured fields. Hutson[26] postulated that dc acoustoelectric current arising from acoustic amplification is generated by equal frequency mixing due to nonlinear effects as exhibited in equation (3.13) below. In terms of the ac component of field and carrier density this is

$$J_a(x) = q \mu \sum_i \tfrac{1}{2} n_i E_i \cos \phi_i \qquad (3.13)$$

where n_i, and E_i are the ac amplitudes of frequency ω_i, and ϕ_i is the relative phase angle. When trapping and diffusion are neglected, McFee*[30] has shown that this equation is equivalent to the Weinreich[34] relation

---

* The author wishes to thank Dr. J.H. McFee of the Bell Telephone Laboratories for an unpublished manuscript dealing with similar results which was used as a guide in interpreting the measurements in this section.

$$J_a(x) = -\frac{\mu}{v_S} \left\langle \frac{dU}{dt} \right\rangle , \qquad (3.14)$$

where U is the acoustic energy density. Using the continuity equation

$$J_i = -q\, v_S\, n_i \qquad (3.15)$$

to eliminate n_i from equation (3.13), he obtains

$$J_a(x) = -\frac{\mu}{v_S} \sum_i \tfrac{1}{2} J_i E_i \cos \phi_i \quad . \qquad (3.16)$$

The summation term in equation (3.16) is the power density supplied by the carriers to the acoustic waves and is identified with $\langle dU/dt \rangle$, the rate of change of acoustic energy density in equation (3.14). Defining the acousto-electric power density, $P_a(x) = \sum_i \frac{1}{2} J_i E_i \cos \phi_i$, equation (3.16) is

$$J_a(x) = -P_a(x) / E_s \qquad (3.17)$$

where $E_s = \frac{v_s}{\mu}$, the field at which electrons have a drift velocity equal to sound velocity. All the equations from equation (3.17) to the end of this section refer to dc steady-state conditions. In regions where there is acoustic gain $P_a(x)$ will be positive, and $J_a(x)$ will subtract from the ohmic current density

$$J_{\Omega}(x) = \sigma(x)\ E(x) \quad , \tag{3.18}$$

but always satisfy the continuity of the total current density

$$J = \sigma(x)\ E(x) - P_a(x)\ /\ E_s \quad . \tag{3.19}$$

From equation (3.19) it follows that the spatial dependence of $\sigma(x)\ E(x)$ and $P_a(x)$ are similar. The conductivity is left dependent on position in order to keep the argument general and concur with observation.

From equation (3.19) the acoustoelectric power density is

$$P_a(x) = (\ \sigma(x)\ E(x) - J)\ E_s \quad . \tag{3.20}$$

It is believed that the measured variations in field can be interpreted as direct evidence of the local build up of acoustic power and that Hutson's postulate leading to equation (3.20) provides a method for its calculation. The field distribution E(x) has been calculated from measurements of the potential distribution for different currents and voltages. Presuming $\sigma(x)$ has been obtained from low voltage results, since E(x) and J are known, $P_a(x)$ and $J_a(x)$ can be calculated. An approximation made by neglecting the conductivity variations with respect to the very rapid field variations leads to

$$P_a(x) \doteq \left[E(x) - IR/L\right] \bar{\sigma} \; E_s \qquad (3.21)$$

where the average conductivity is $\bar{\sigma}$ and $R = L/\bar{\sigma}A$ the sample's low voltage resistance. The values of field from Figure (3.10) and the measured current were substituted into equation (3.21) to calculate the location where $P_a = 0$, the net acousto-electric power, and the values of E, P_a and I_a at probe strip position 1.

For this sample $E_s = 575$ v/cm,

$\bar{\sigma} = 10^{-4}\ (\Omega\,\mathrm{cm})^{-1}$, and

$R = 110\ \mathrm{K}\Omega$.

The table below lists the results found for four values of applied voltage.

Applied Volts	Current I (mA)	Joule Power I^2R(W)	IR/L v/cm	Location of $P_a=0$	Total Acousto-electric Power(W)	E(1) v/cm	$I_a(1)$ mA	$P_a(1)$ W/cc
2000	9.2	9.4	1000	7	6	4000	-30	170
1550	8.5	8	890	6	4	3400	-25	144
1200	7.2	5.7	790	6	2.4	2500	-17	98
750	6.2	4.2	670	5	0.5	1300	-6.3	37

From the above results the following was concluded:

1) For the distribution of Figure 3.10 the point where $P_a = 0$ divided the crystal into an amplifying region near the anode and an attenuating region near the cathode.

2) The net acoustoelectric power, obtained from the net area between the field distribution and the datum level IR/L,

was comparable to the Joule power for voltages appreciably in excess of the saturation value.

3) The acoustoelectric current in the high field regions exceeded the circuit current.

4) As the voltage was increased a larger portion of the crystal was in an amplifying state.

To include conductivity variations it is only necessary to scale the field measurements by the ratio $\sigma(x)/\bar{\sigma}$ before proceeding as above.

The results showed that there was always a net acoustoelectric power whenever the voltage was above the saturation value, and a somewhat simpler way was found to calculate this. Integrating equation (3.19) over the crystal volume, the current-voltage characteristic for the sample is

$$I = GV - \frac{1}{V_S} \int_{vol} P_a dv \qquad (3.22)$$

where $G = \bar{\sigma}A/L$, $V_S = E_s L$, and $V = \int_0^L E(x)\, dx$, the terminal voltage. Equation (3.22) predicts a current less than ohmic whenever there is a net power supplied by the carriers to the acoustic waves. The onset of saturation occurs when amplification starts, since only then will there be a significant increase in the integral of equation (3.22). We obtain the net acoustoelectric power

$$\int_{vol} P_a dv = (GV - I)V_S = (V - IR)I_s \quad , \qquad (3.23)$$

where $I_s = G\ V_S$ the saturation current, directly from the terminal current-voltage characteristic of the sample as shown in Figure 3.13.

For a sample exhibiting an ideal saturation characteristic, neglecting conductivity variations, this datum line becomes independent of voltage and equal to the critical field E_s and whenever $E(x) = E_s$, $P_a(x) = 0$ in agreement with the linear amplification theory which requires $\phi_i = 90^\circ$ at the critical field. The results obtained however show that $E(x) > E_s$ when $P_a(x) = 0$, and it is likely that non-electronic losses and trapping need to be included in a more detailed theory.

In summary, the non-uniform field distributions measured were interpreted in terms of a steady state acousto-electric power density distribution as outlined by McFee. When net power was taken from the carriers by the acoustic waves, it was calculated from the current-voltage

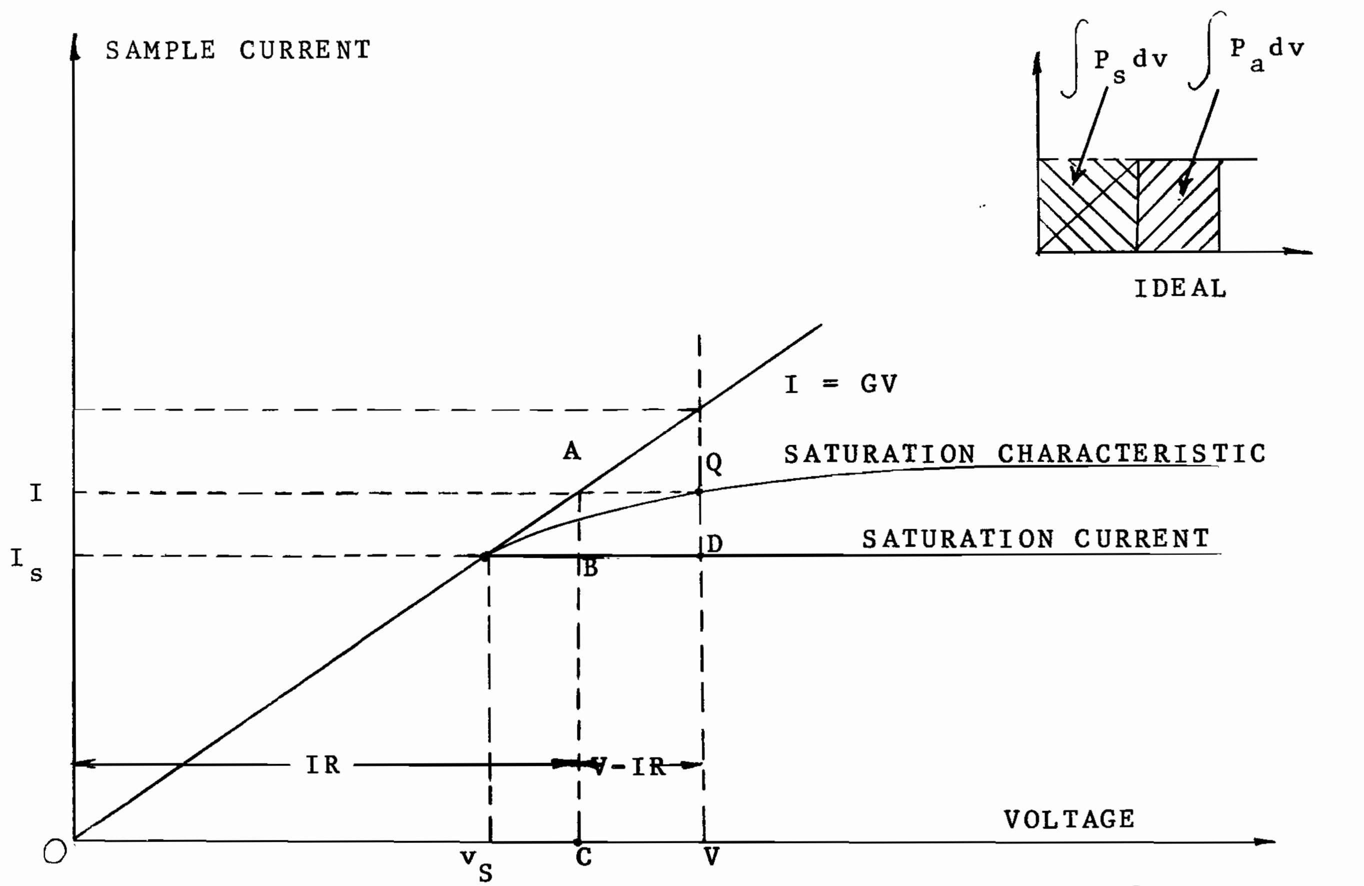

TOTAL INPUT POWER $= \int_{vol} P_T dv =$ AREA OIQV

ACOUSTOELECTRIC $\int_{vol} P_a dv =$ CBDV

JOULE HEATING $= \int_{vol} P_j dv =$ OIAC

EXCESS LOSS $W_E =$ BAQD

FIGURE 3.13 CALCULATION OF ACOUSTOELECTRIC POWER characteristic of the sample but the details of its distribution were only obtained from the potential profiles. The main role of conductivity variations was to determine the detailed distribution of field as can be seen by contrasting the results obtained on reversal of current shown in Figure 3.10 and Figure 3.12. McFee divides his sample into two different conductivity regions and predicts a saturation characteristic by assuming that the rate of acoustic energy growth in one region is balanced by the rate of acoustic loss in the other region. Equation (3.22) is an equivalent statement of saturation in terms of a net acoustic power over the entire sample.

CHAPTER IV

CURRENT INSTABILITIES IN CdS

4.1 Introduction

With applied voltages exceeding those required for acoustic amplification, oscillations in the current are observed. These occur under conditions of both uniform and non-uniform illumination and can have an almost sinusoidal waveform. Mechanisms proposed to account for them have been qualitative and invoked the idea of acoustic round trip gain in the sample[9,11,12].

Oscillations, easily generated when the anode end was masked, were apparently triggered by increasing the field in precisely the region where it increased due to the growth of acoustoelectric flux. With fairly intense illumination oscillations were observed almost immediately upon application of the drift pulse, but low intensity uniform illumination built up continuous oscillations over a fairly long time and were only observed when a long enough drift pulse was applied. This type remained undamped over a narrow illumination range.

4.2 Type I Instabilities - Non-Uniform Illumination

4.2.1 Measurements and Results

Measurement of the oscillation frequency was made using the comparison circuit shown in Figure 4.1. The phase and frequency of the sinusoidal generator were adjusted to get coincidence over 20 or more cycles so that the counter indicated the frequency. The procedure, though tedious, produces results which are accurate to better than 1%.

This frequency was measured for different applied voltages, illuminations, and circuit impedances, and the results for one sample, Har#2, are pictured in Figures 4.2 - 4.5. In Figure 4.2 constant voltage mode curves show the frequency of oscillation with zero series impedance varying with the conductance of the sample; there is a 3 mm. mask at the anode end. For almost all the loci plotted the frequency, covering a two-to-one change, increases with the conductivity; and the voltage dependence is small. Figure 4.3 depicts the same data as constant conductance mode curves, thereby focussing attention on the fact that the voltage sensitivity changes sign at a certain conductivity. The effect of series impedance was measured, and it was found that the frequency could be significantly pulled by it. Figure 4.4, Curves A, B, and C illustrate this phenomenon for three values of sample resistance. The oscillation obtained corresponding to the

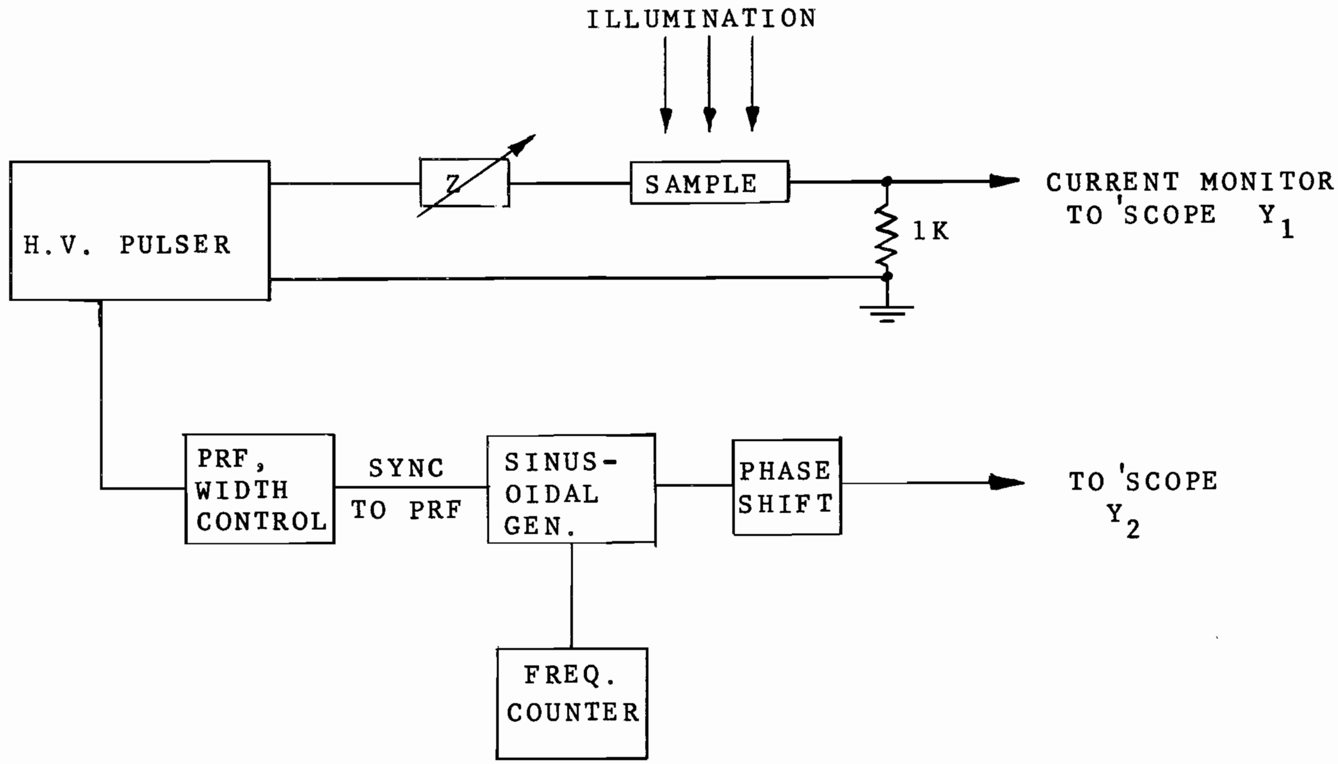

FIGURE 4.1 FREQUENCY MEASURING CIRCUIT

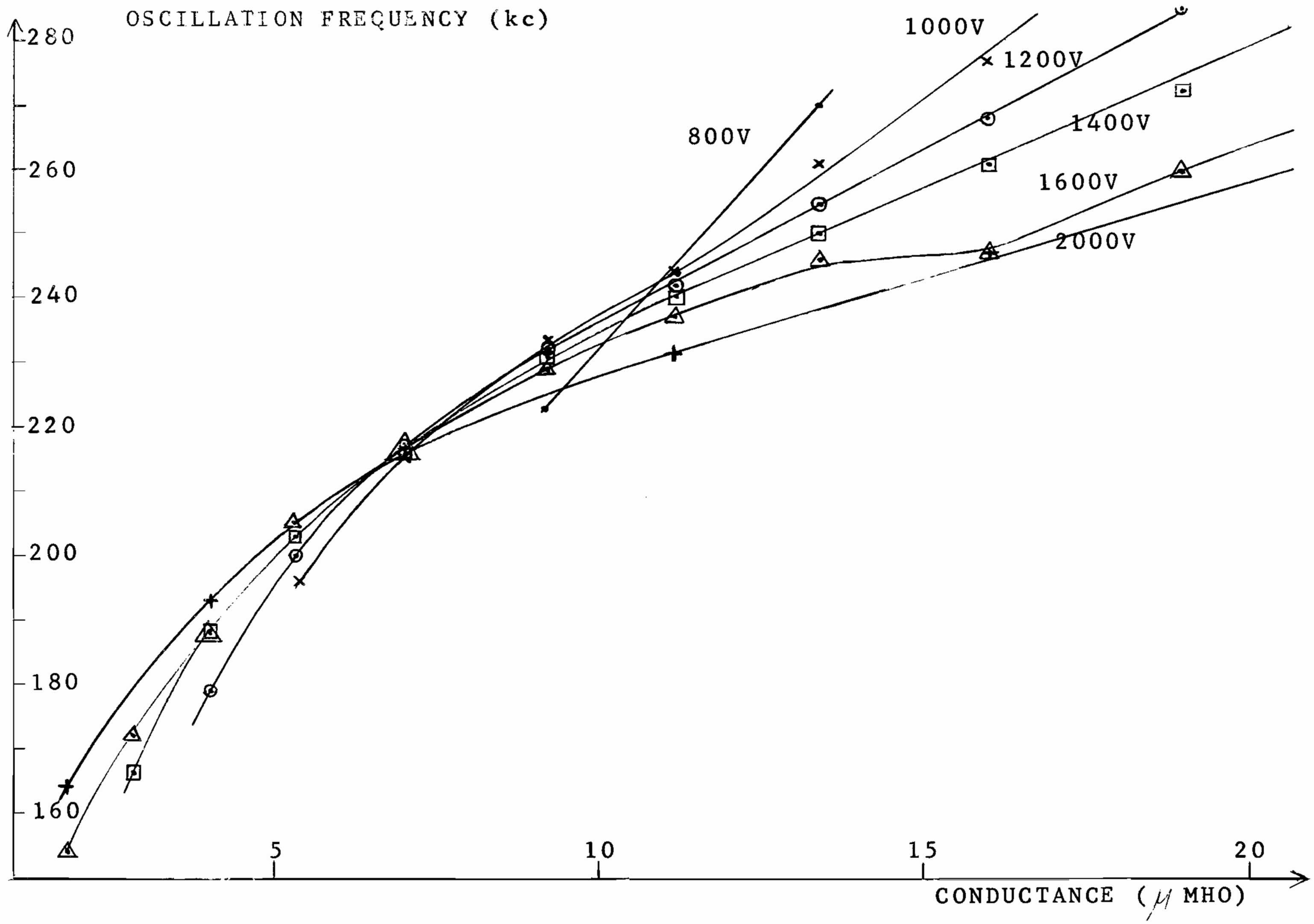

FIGURE 4.2 CONSTANT VOLTAGE LOCI FOR OSCILLATIONS IN SAMPLE HAR#2, 3 MM MASK AT ANODE

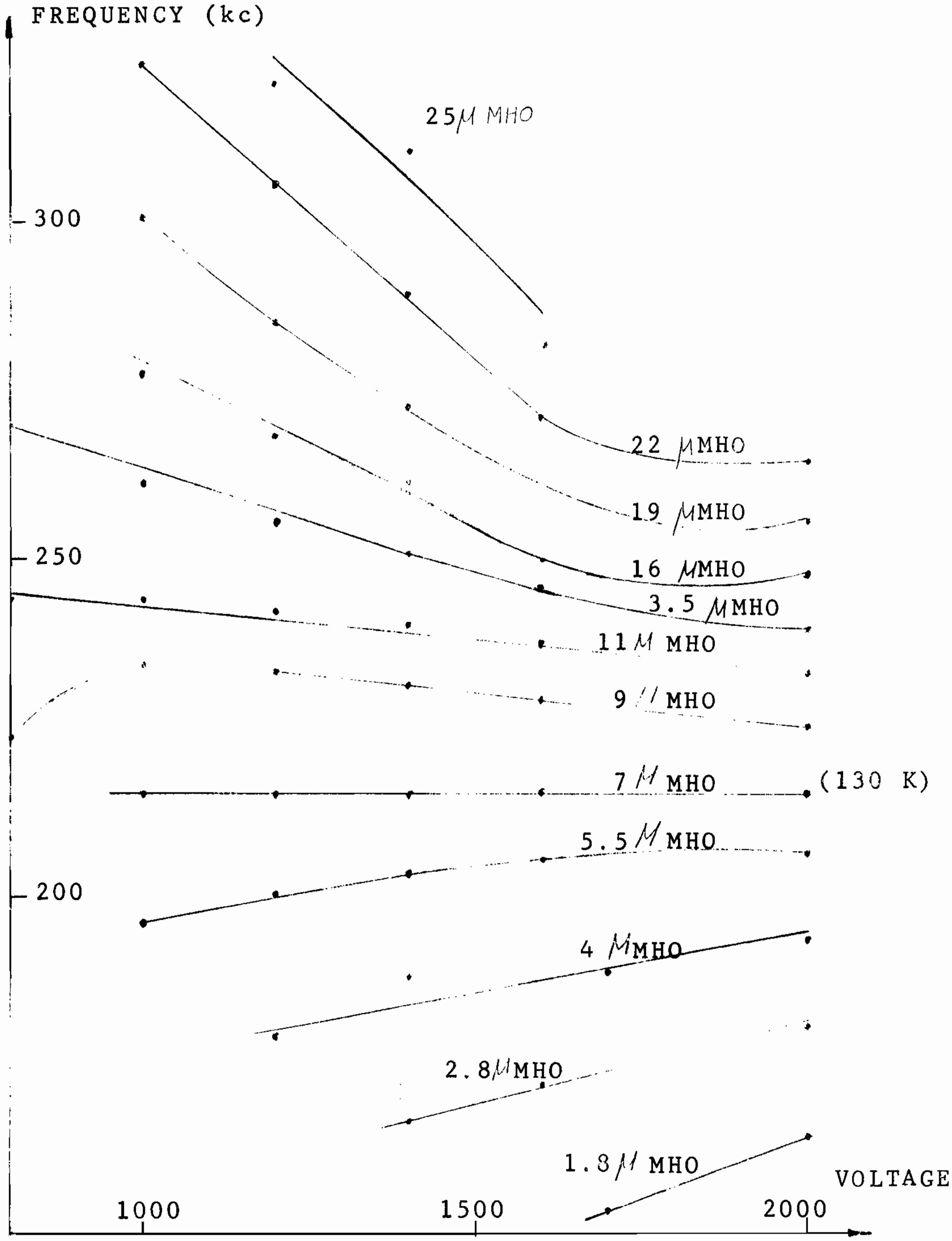

FIGURE 4.3 CONSTANT CONDUCTANCE LOCI FOR OSCILLATIONS IN HAR#2, 3 MM MASK AT ANODE

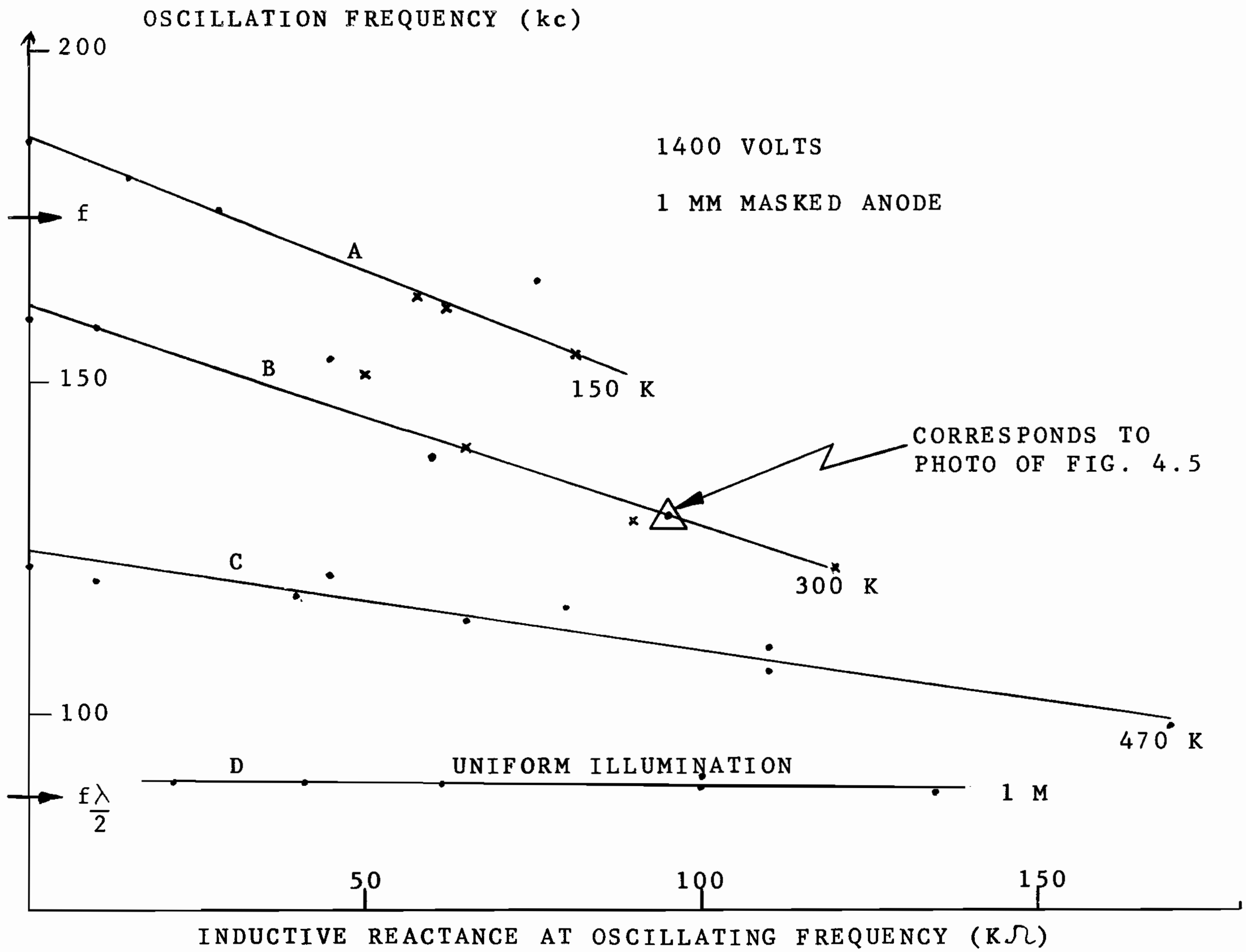

FIGURE 4.4 FREQUENCY OF OSCILLATION VS REACTANCE
FOR DIFFERENT ILLUMINATIONS FOR SAMPLE Har#2

point Δ on Curve B is depicted in Figure 4.5.

In another experiment with sample EP1#3 in an amplifier assembly current oscillations and an output from the transducers at the same frequency were recorded indicating the presence of mechanical oscillations.

4.2.2 Discussion of Results

The significant dependence of the frequency of oscillation demonstrated in all the measurements makes it difficult to accept an interpretation based on the reflection of acoustic waves between the end faces. Providing there was enough gain, the frequency would not be effected by voltage or external impedance, since one would then expect the half wavelength frequency and its odd harmonics to dominate; namely $88 \cdot (2n + 1)$ kc for the 1 cm. bar. It is more likely that these oscillations are caused by unstable high field domains as discussed by Ridley[31].

The existence of stable high field domains at the anode of an unmasked sample have been discussed, but masking the anode produced current oscillations. It seems that this increases the field to the point where these domains become unstable, and capacitive probe measurements[32] have shown evidence of their propagation, disappearance and regeneration.

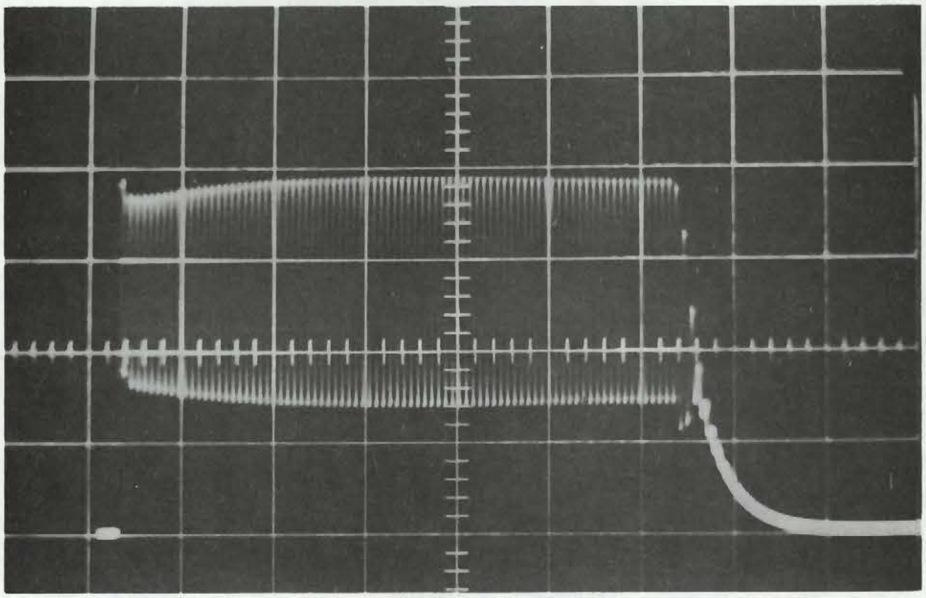

FIGURE 4.5 Current oscillations with anode masked. Vertical scale, 1 mA/cm; horizontal scale, 100 μs/cm; frequency of oscillation, 130 kc; illumination, 23 fc, 10 per cent masking; field, 1400 V/cm.

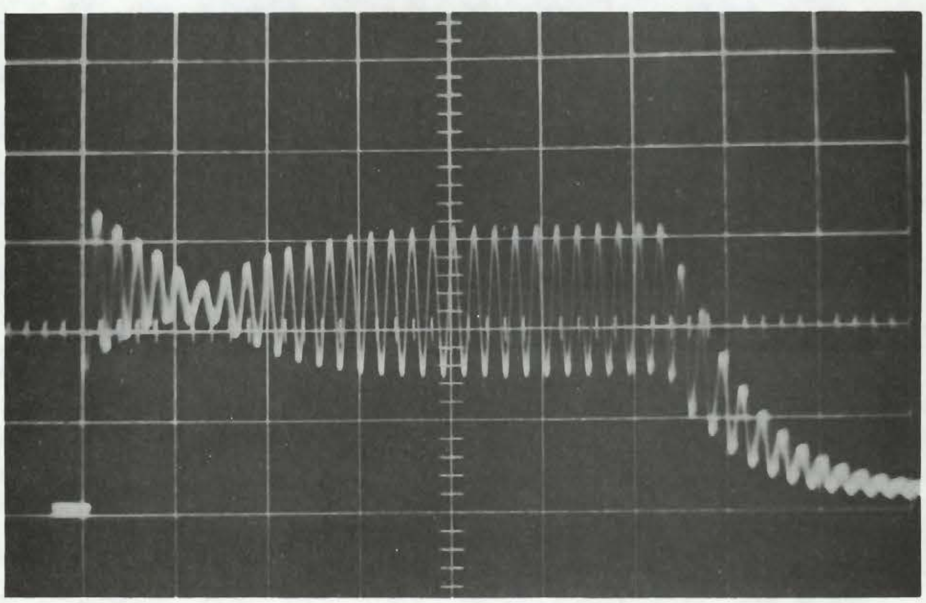

FIGURE 4.6 Current oscillations with uniform illumination of 7.6 fc. Vertical scale, 0.5 mA/cm; horizontal scale, 50 μ s/cm; frequency of oscillation, 88.8 kc.

The mechanism causing this instability in CdS is not known, but from the results it can be seen that a negative conductivity gradient near the anode is a critical factor.

4.3 Type II Instabilities - Uniform Illumination

4.3.1 Measurements and Results

When the sample illumination was uniform, oscillations with no measurable change in frequency due to external impedance and remarkably close to the half wavelength value were observed. Measurements on sample Har#2 as a function of external impedance are shown in Figures 4.4 and 4.7, Curve D. This was obtained with a 1400 volt drift pulse at an illumination of 7.6 fc. A change in voltage from 1200 to 2200 produced no measurable frequency change, and outside of this range the oscillations were either heavily damped or ceased completely. They also disappeared if the illumination was above 8.6 fc or decreased below 7.0 fc. Figure 4.6 is an oscillograph with the same conditions of illumination and field as Curve D, Figure 4.7 and an inductance of 0.24 henry in series.

4.3.2 Interpretation of Results

The constancy of the frequency of oscillation in these instabilities, the independence on external circuitry and

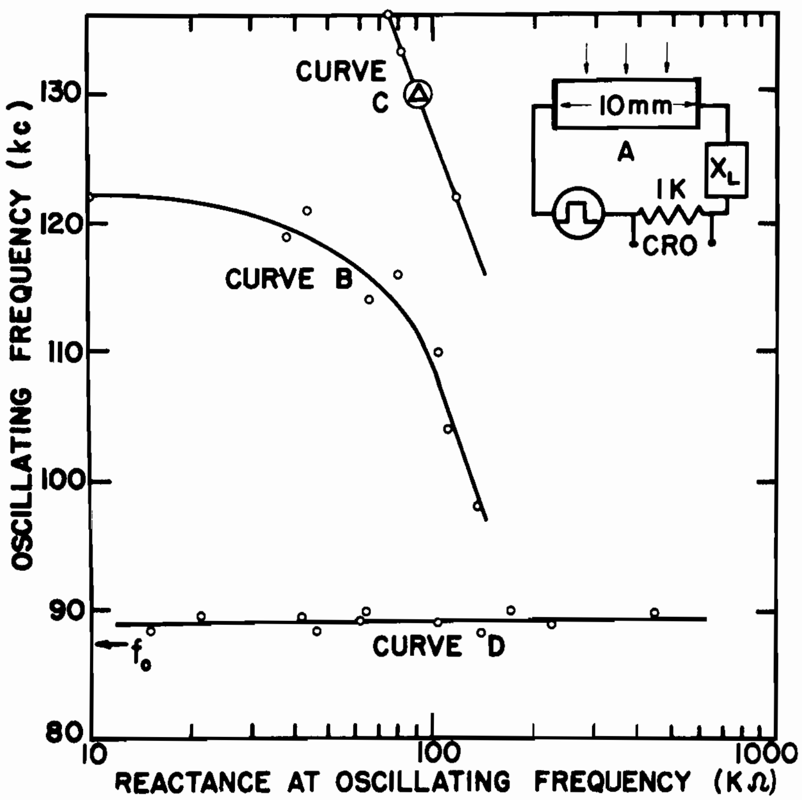

FIGURE 4.7 A: Outline of circuit, Curve B: Frequency vs. reactance for 1-mm mask at anode. Illumination, 16 fc; field, 1400 V/cm. Curve C: Same as for curve B, except that illumination is 23 fc. Curve D: Frequency vs. reactance for illumination, 7.6 fc; field, 1400 V/cm.

voltage, and the value of the oscillation frequency is attributed to a negative resistance effect caused by the acoustic gain mechanism. A linear theory has been developed which predicts this effect.

4.4 The Electrical Impedance of a Biased CdS Bar

4.4.1 Introduction

If the acoustic gain is directly responsible for the observed oscillations, then inclusion of the contributions of the growing acoustic waves in calculations of the terminal impedance of a suitably biased CdS bar should yield a negative resistance regime[14]. The analysis below focusses attention onto these contributions, and numerical results for CdS under various bias and conductivity conditions do indeed show such negative resistance.

4.4.2 Basic Equations

Considering plane waves in an n-type piezoelectric semiconductor, two sets of equations need to be satisfied simultaneously. Following the notation used by Hutson and White[2,3], the first set is the piezoelectric equations of state:

$$T = cS - eE \tag{4.1}$$

$$D = eS + \epsilon E \tag{4.2}$$

where T and S are the stress and strain, D and E the electric displacement and field, c the elastic constant at constant field, ϵ the permitivity at constant strain and e the piezoelectric constant. Since the coupling to be considered is one dimensional the variables in the above equations are scalars and for a medium displacement U, $S = \partial U/\partial x$. The equation of motion is

$$\rho \, \partial^2 U/\partial t^2 = \partial T/\partial x \tag{4.3}$$

where ρ is the mass density.

The second set of equations (4.4), (4.5), and (4.6) follow from Maxwell's equations and the constitutive equations for the medium.

$$\partial D/\partial x = Q \tag{4.4}$$

$$\partial J/\partial x + \partial Q/\partial t = 0 \tag{4.5}$$

$$J = \sigma E + qD_e \, \partial n_s/\partial x \tag{4.6}$$

where J is the current density, Q the space charge, σ the conductivity, q the magnitude of the electronic charge, D_e the diffusion constant for electrons and n_s the varying component of free-electron density in the conduction band.

It has been assumed that there is no trapping. Equation (4.6) is valid for angular frequencies much less than the reciprocal of the electron-lattice relaxation time. The conductivity is then given by

$$\sigma = \mu q(n_o + n_s) \tag{4.7}$$

in which μ is the electron mobility and n_o is the equilibrium free-electron density. Since the medium is electrically neutral in equilibrium, the space charge $Q = -qn_s$.

Equations (4.4), (4.5) and (4.7) are used to eliminate all variables except D and E from equation (4.6) the resultant equation being

$$\partial^2 D/\partial x\, \partial t + \frac{\partial}{\partial x}\left[(\sigma_o - \mu \partial D/\partial x) E \right] - D_e\, \partial^3 D/\partial x^3 = 0 \tag{4.8}$$

where $\sigma_o = \mu q n_o$ is the equilibrium conductivity.

For a single plane wave component, the displacement of the medium is assumed to be

$$U(x, t) = U_1 e^{i(kx - \omega t)} \tag{4.9}$$

with a similar representation for T. The electric field is taken to be

$$E(x,\ t) \ = \ E_{DC} + E_1 e^{i(kx\ -\ \omega t)} \qquad (4.10)$$

Using equation (4.9) and equation (4.10) in equations (4.1), (4.2), (4.3) and (4.8) results in a set of homogeneous equations in the plane wave amplitudes T_1, U_1, D_1 and E_1. These are written for convenience in matrix form after having neglected the harmonics and dc terms generated by mixed products[2] in equation (4.8).

$$\begin{bmatrix} 1 & -ick & e & 0 \\ 0 & iek & \epsilon & -1 \\ ik & \rho\omega^2 & 0 & 0 \\ 0 & 0 & ik\sigma'_o & \omega k + \mu E_{DC}k^2 + ik^3 D_e \end{bmatrix} \times \begin{bmatrix} T_1 \\ U_1 \\ E_1 \\ D_1 \end{bmatrix} = 0 \qquad (4.11)$$

By setting the determinant equal to zero, one obtains the dispersion relation which becomes a quartic in k after removing a common k term originating from equation (4.8). This quartic may be written as:

$$\left[\omega + \mu E_{DC} k + i k^2 D_e + (i\, \sigma_o / \epsilon) \right] \left[k^2 - \rho \omega^2 / c \right]$$

$$+ \frac{e^2}{\epsilon c} k^2 \left(\omega + \mu E_{DC} k + i k^2 D_e \right) = 0 \qquad (4.12)$$

which is essentially the equation (5) in the paper by Parsons[33].

The solution of the quartic yields four allowed waves, two quasi-acoustic and two quasi-carrier waves. The acoustic wave travelling in the direction of the electrons is amplified when the drift velocity is supersonic, whereas the other three waves are attenuated.

4.4.3 Propagation of Acoustoelectric Waves

From equations (4.1) and (4.3) one obtains the wave equation

$$\rho\, \partial^2 U / \partial t^2 = c\, \partial^2 U / \partial x^2 - e\, \partial E / \partial x \qquad (4.13)$$

from which, for any plane wave component E_j corresponding to a wave vector k_j, it follows that

$$E_j = (ic/e)(k_j - \omega^2 / v_s{}^2 k_j) U_j \qquad (4.14)$$

with $v_s = (c/\rho)^{1/2}$ the velocity of sound at constant field.

When all waves are present as in a bar of finite length, the total material displacement becomes

$$U = \sum_{j=1}^{4} U_j e^{ik_j x} \tag{4.15}$$

The total electric field is written as:

$$E(x, t) = E_{DC} + E_o e^{-i\omega t} + \sum_{j=1}^{4} E_j e^{i(k_j x - \omega t)} \tag{4.16}$$

where E_{DC} is the field due to an applied dc voltage, E_o the field due to an applied ac voltage and $\sum_{j=1}^{4} E_j e^{i(k_j x - \omega t)}$ the field due to the four travelling waves. From equations (4.14) and (4.15) the ac electric field is

$$E = E_o + (ic/e) \sum_{j=1}^{4} (1 - \omega^2/v_s{}^2 k_j{}^2) k_j U_j e^{ik_j x} \tag{4.17}$$

in which the time dependence $e^{-i\omega t}$ is understood, and the summation is over the four wave vectors. The strain and stress follow from equations (4.1) and (4.15)

$$S = \sum ik_j U_j e^{ik_j x} \tag{4.18}$$

$$T = -eE_o + (ic\,\omega^2/v_s^2) \sum (U_j/k_j)\,e^{ik_jx} \tag{4.19}$$

Also from equations (4.2) and (4.6) $D = \epsilon E_o + D(x)$ and

$$J = \sigma_o E_o + J(x)$$

where $D(x)$, $J(x)$ are the contributions due to the four waves. The external circuit current J_o can be only time dependent not space dependent, $J_o = (J - i\omega D)$. From Maxwell's curl equation for this one-dimensional problem $J(x) - i\omega D(x) = 0$ for all x and from this it follows that

$$J_o = (\sigma_o - i\,\omega\epsilon)\,E_o \tag{4.20}$$

4.4.4 <u>The Electrical Impedance</u>

From equation (4.17) the total ac voltage across a length L of a crystal will be given simply by

$$V = \int_o^L E\,dx = E_o\left[L + \sum_{j=1}^{4} (cU_j/eE_o)(1 - \omega^2/v_s^2\,k_j^2)(e^{ik_jL}-1)\right]$$

(4.21)

The external current I_o is given by equation (4.20) hence the impedance Z will be V/I_o

$$Z = \frac{L + \sum_{j=1}^{4} (cU_j/eE_o)(1 - \omega^2/v_s{}^2\ k_j{}^2)(e^{ik_jL} - 1)}{\sigma_o A(1 - i\,\omega\epsilon/\sigma_o)}$$

(4.22)

where A is the cross section of the bar. Equation (4.22) is in effect the general expression for the impedance of the piezoelectric bar. By applying appropriate boundary conditions, the amplitudes U_j of the medium displacement can be evaluated and the impedance expressed as a function of the k_j, the conductivity, the sample dimensions and the frequency. A convenient normalization which is useful for computational purposes is obtained by defining $\lambda_j = cU_j/eE_o$ and $R_o = L/\sigma_o A$ to get

$$Z/R_o = \frac{1 + \sum(\lambda_j/L)(1 - \omega^2/k_j{}^2\ v_s{}^2)(e^{ik_jL} - 1)}{1 - i\,\omega\epsilon/\sigma_o}$$

(4.23)

4.4.5 Boundary Conditions

In a medium of finite length the waves described in Section 4.4.3 and 4.4.4 will be excited by an externally applied ac voltage and their amplitudes and distribution in space will be determined by the boundary conditions. In the present one-dimensional model, the sample length "L" gives the positions of the physical boundaries. It is assumed that the bar is stress free at the ends, which condition is stated as:

$$T(0) = T(L) = 0 \tag{4.24}$$

From equation (4.1) this implies for the ac part

$$\begin{aligned} S(0) - eE(0)/c &= 0 \\ S(L) - eE(L)/c &= 0 \end{aligned} \tag{4.25}$$

Equations (4.17) and (4.18) evaluated at x = 0 and x = L yield

$$S(0) = \sum ik_j U_j$$

$$S(L) = \sum ik_j U_j e^{ik_j L} \tag{4.26}$$

$$E(0) = E_o + (ic/e) \sum (1 - \omega^2/v_s^2\, k_j^2) k_j U_j$$

$$E(L) = E_o + (ic/e) \sum (1 - \omega^2/v_s^2\, k_j^2) k_j U_j e^{ik_j L}$$

$$\tag{4.27}$$

for the ac part.

Substituting equations (4.26) and (4.27) into equation (4.25) these boundary conditions imply that

$$\sum i\omega^2 \lambda_j / v_s^2 k_j = 1$$

$$\sum (i\omega^2 \lambda_j / v_s^2 k_j) e^{ik_j L} = 1 \qquad (4.28)$$

The Two-Wave Approximation

The conditions specified by equation (4.28) are sufficient to evaluate approximately the impedance function equation (4.22). The approximation involved is to assume simply that the quasi-acoustic waves are dominant and to neglect the quasi-carrier waves completely. Studies of the roots of the quartic show that the backward (in the sense of against the electrons) carrier wave is very strongly damped and in fact if one neglects diffusion would not exist because the dispersion relation becomes cubic. Typically the attenuation of this wave is 20,000 nepers per centimetre irrespective of frequency for drift velocities of the order of sonic velocities. This wave can obviously be completely neglected.

Studies of the properties of the forward carrier wave show that it is attenuated at the rate of approximately 3 nepers per wavelength and therefore can be neglected only for samples which are many acoustic wavelengths long.

For long samples it is possible to obtain a simple equation for the impedance by solving equations (4.26) and (4.27) to yield the following values for λ_1, λ_2.

$$\lambda_1 = (v_s^2 k_1 / i\omega^2)(e^{ik_2L} - 1)/(e^{ik_2L} - e^{ik_1L})$$

$$\lambda_2 = (v_s^2 k_2 / i\omega^2)(1 - e^{ik_1L})/(e^{ik_2L} - e^{ik_1L}) \tag{4.29}$$

Substituting these values into equation (4.23) the impedance is found to be

$$Z/R_o = \frac{1 + \left(\frac{1}{iL}\right)\left[\frac{v_s^2}{\omega^2}(k_1 - k_2) - \frac{1}{k_1} + \frac{1}{k_2}\right]\left[\frac{(e^{ik_2L} - 1)(e^{ik_1L} - 1)}{e^{ik_2L} - e^{ik_1L}}\right]}{1 - i\omega\epsilon/\sigma_o} \tag{4.30}$$

Equation (4.30) is then the two-wave approximation to the impedance function.

The Three-Wave Calculation

To obtain the impedance for lower frequencies it is necessary to include the effect of the forward carrier wave thus requiring an additional boundary condition to solve for the three λ's needed. As a reasonable boundary condition the plane wave component of either the space charge or the current density is made to vanish at the cathode end of the bar. Such a choice may be thought of as defining an ideal metallic contact at the cathode. Setting the current density equal to zero yields as another boundary condition

$$\sum (1 + e^2/\epsilon c - \omega^2/v_s^2 k_j^2)\, i k_j U_j = 0 \qquad (4.31)$$

while setting the space charge density equal to zero gives

$$\sum (1 + e^2/\epsilon c - \omega^2/v_s^2 k_j^2)\, k_j^2 U_j = 0 \qquad (4.32)$$

Either of the above equations seem reasonable and computations show negligible difference between the results obtained for these two conditions.

4.4.6 A Proof that the Impedance Loci are Circular

The loci are circular over the narrow resonant region. The impedance can be written

$$Z = Z_o + \frac{Z_o(k_1 - k_2)}{iLk_1k_2}\left[\frac{v_S{}^2}{\omega^2} k_1k_2+1\right]\frac{(e^{-ik_2L}-1)(e^{ik_1L}-1)}{(e^{i(k_1-k_2)L} - 1)}$$

(4.33)

where $Z_o = R_o / (1 - i\omega\sigma/\epsilon)$.

In any narrow frequency interval near one of the mechanical resonances it can be shown that the only term in equation (4.33) which changes significantly is the term, D, in the denominator, defined by

$$D = e^{i(k_1 - k_2)L} - 1 \quad . \tag{4.34}$$

Writing

$$i(k_1 - k_2)L = i\omega L(1/v_1 + 1/v_2) - (\alpha_1 + \alpha_2)L \tag{4.35}$$

and defining a resonance by

$$\omega_o L\ (1/v_1 + 1/v_2) = 2\pi\ (2n + 1),\ n = 0,1,\ldots \qquad (4.36)$$

and a frequency deviation by

$$\omega = \omega_o(1 + \Delta f/_{fo}) \qquad (4.37)$$

Equation (4.36) can be written

$$i(k_1 - k_2)L = i2\pi(2n + 1)(1 + \Delta f/_{fo}) - (\alpha_1 + \alpha_2)L\ . \qquad (4.38)$$

Substituting in equation (4.34)

$$D(\Delta f) = e^{i2\pi(2n + 1)\ \Delta f/_{fo} - (\alpha_1 + \alpha_2)L} - 1\ . \qquad (4.39)$$

Since $(\alpha_1 + \alpha_2)L \ll 1$, if $2\pi(2n + 1)\ \Delta f/_{fo} \ll 1$, this can be expanded retaining only first order terms

$$D(\Delta f) = i2\pi(\Delta f/_{fo})(2n + 1) - (\alpha_1 + \alpha_2)L\ . \qquad (4.40)$$

The impedance can now be written

$$Z = Z_o + Z_o^{1} \;/\; -(\alpha_1 + \alpha_2)L + i2\pi \,\Delta f/_{fo}\,(2n + 1).$$

(4.41)

This denominator exhibits well known resonant circuit behaviour

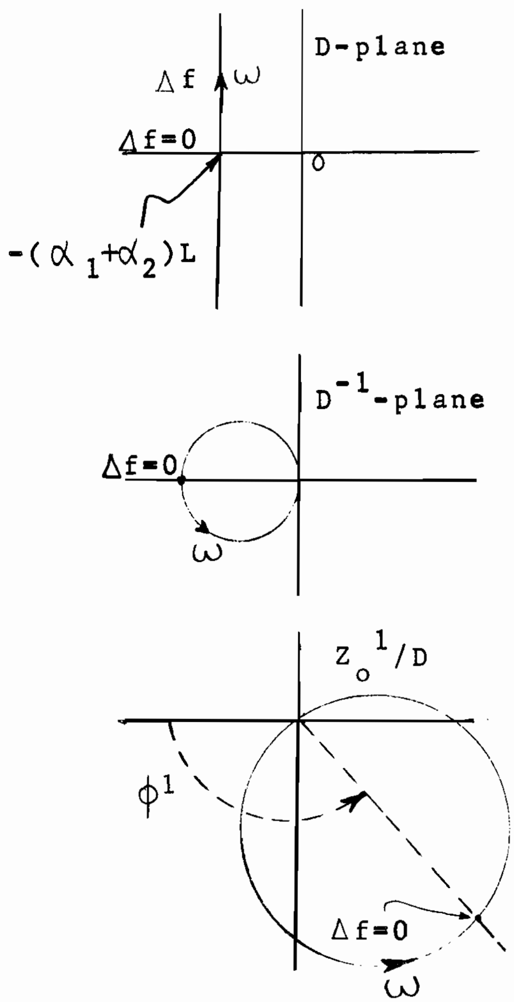

The D locus will be a vertical line in the complex plane going through the real point $-(\alpha_1 + \alpha_2)L$ at $\Delta f = 0$. The mapping of D^{-1} will be a circle in the complex plane, and therefore, the locus of Z_o^{1}/D will be a circle.

If we write $Z_o^{1} = \left| Z_o^{1} \right| e^{i\phi^{1}}$, this will be a rotation of the D^{-1} circle with diameter $\left|Z_o^{1}\right| / \left|(\alpha_1 + \alpha_2)\right| L$.

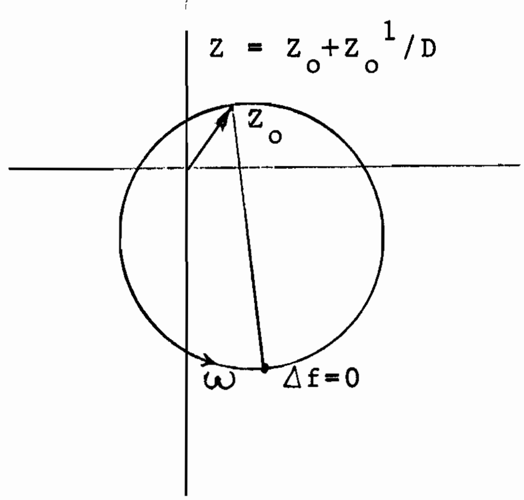

Finally, to get the locus of Z this last circle is translated by an amount Z_o.

The bandwidth of this resonant behaviour follows from equation (4.40) as the value of Δf which makes $D(\Delta f)$ twice $D(0)$.

$$\text{Bandwidth} = \left|(\alpha_1 + \alpha_2)\right| Lf_o / \pi (2n + 1) \quad . \qquad (4.42)$$

This shows that the resonance becomes sharper at higher harmonics, or when the round trip gain is close to unity.

4.4.7 Results of Computations

The impedance has been calculated for low frequencies corresponding to the fundamental and low harmonic resonances for a 1 cm bar with the bar conductivity and the carrier drift velocity as running parameters. These calculations used both the two-wave and the three-wave formulations described in Section 4.4.5.

A typical set of impedance loci calculated in the region where the bar is approximately 2.5 wavelengths long (called fifth harmonic) is plotted in Figure 4.8 for a drift velocity which is twice the sound velocity. The solid curves are the two-wave case whereas the broken curves are the three-wave case for which zero space charge at the cathode has been used as the third boundary condition. It is seen that the loci are circular over the 1% frequency range plotted and that for some values of conductivity the loci enter the left half plane, i.e. the bar exhibits negative resistance. Outside this range the impedance is more or less independent of frequency. The main difference between the two-wave and the three-wave results is that similar loci occur at slightly different conductivities. This behaviour is characteristic of the third and higher harmonics and by the time the seventh harmonic is reached there is almost no difference between the two and three-wave results. This comparison is shown in Figure 4.9 where the two-wave and three-wave calculations are contrasted. At the fundamental frequency there is 0.5% difference in the location of the resonant peak and a large difference in the amplitude;

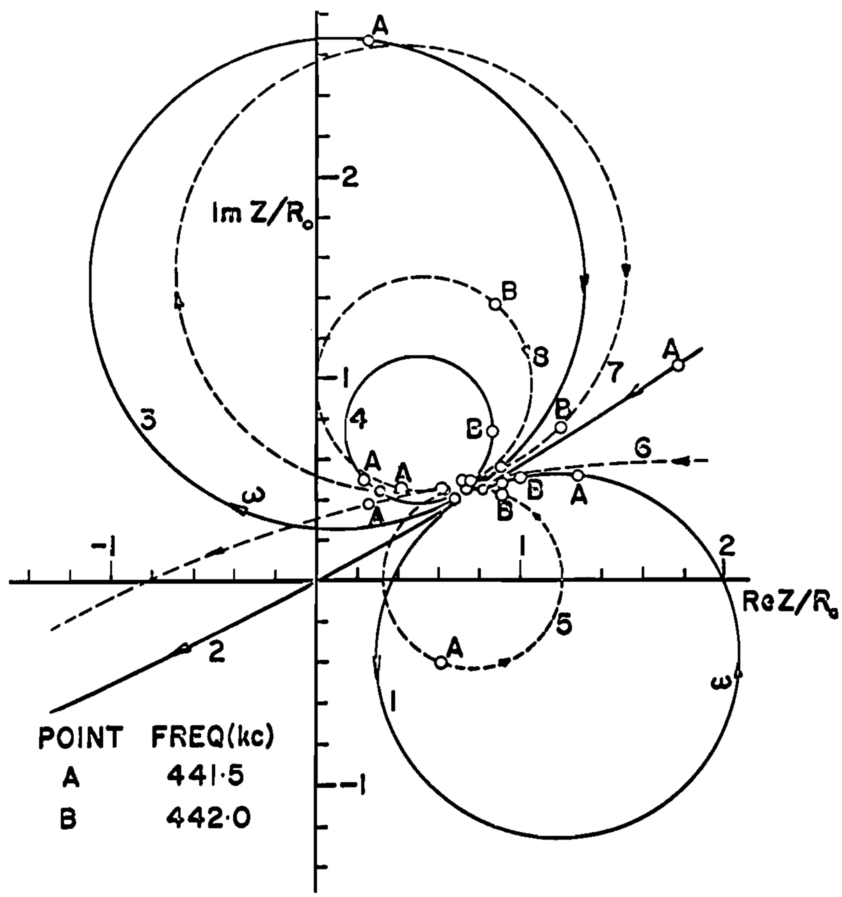

FIGURE 4.8 Fifth harmonic impedance loci for $v_D = 2v_S$. All curves start at 440 kc and end at 443 kc. The two-wave results are shown solid, the three-wave broken. Conductivities are 4.02, 3.87, 3.77, 3.5, 3.5, 3.26, 3.14 and 3.01 $(\text{megohm cm})^{-1}$ for curves 1 through 8 respectively.

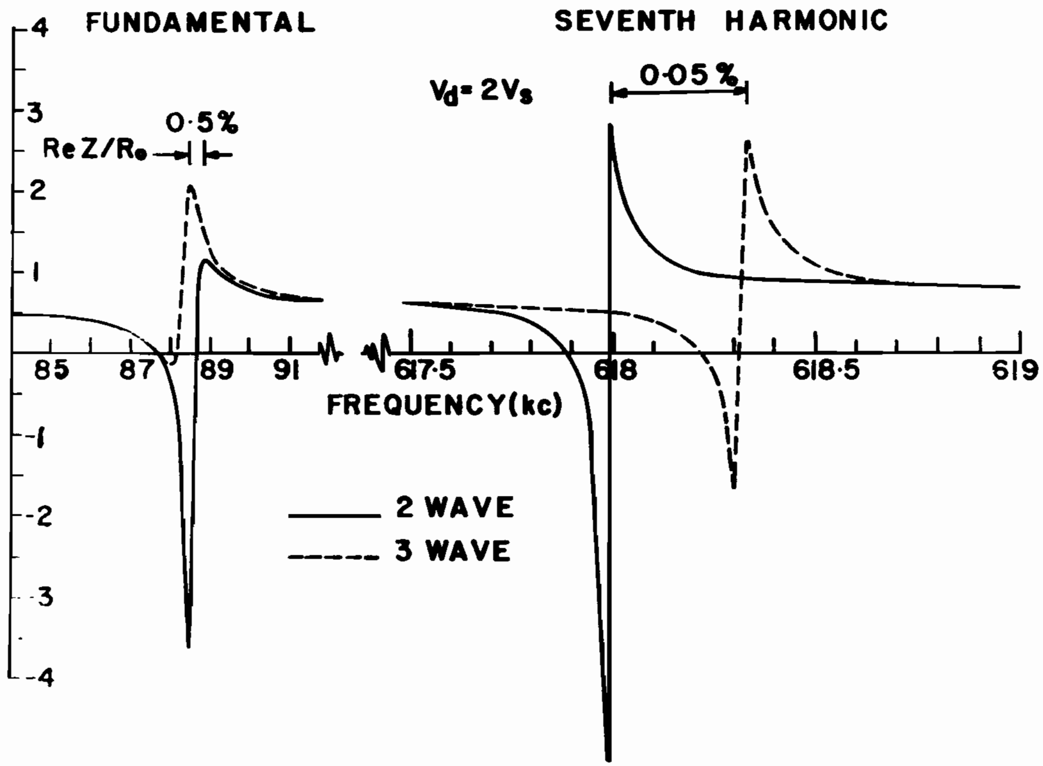

FIGURE 4.9 Fundamental and Seventh harmonic calculation comparing three-wave and two-wave calculations for the same conductivity showing closer agreement for the seventh harmonic compared to fundamental.

whereas at the seventh harmonic the resonant separation is only 0.05% and the amplitudes are comparable.

Setting the electrical displacement zero at the cathode as an alternative test boundary condition does not change the three-wave results perceptibly.

At the fundamental mode the impedance lòci are quite different for the two calculations. The two-wave calculation is shown in Figure 4.11 and the behaviour is seen to be very similar to the results for the fifth harmonic. However, the three-wave loci in Figure 4.12 are qualitatively diffèrent, in particular the loci do not exhibit the change in the sense of encirclement which is characteristic of the other results. This indicates the result of taking into account the third-wave at the low harmonics.

In Figure 4.13 the real part of the impedance is plotted as a function of frequency for the fundamental, third and seventh harmonics with the imaginary part for the fundamental shown by the broken curve. This representation demonstrates how sharp the resonances are.

The influence of drift velocity is illustrated in Figure 4.14 for the seventh harmonic. For a given conductivity which gives negative resistance at $v_D = 2v_S$ the negative resistance has disappeared at values of drift velocity just 5% above and below $2v_S$. In contrast to these low frequency

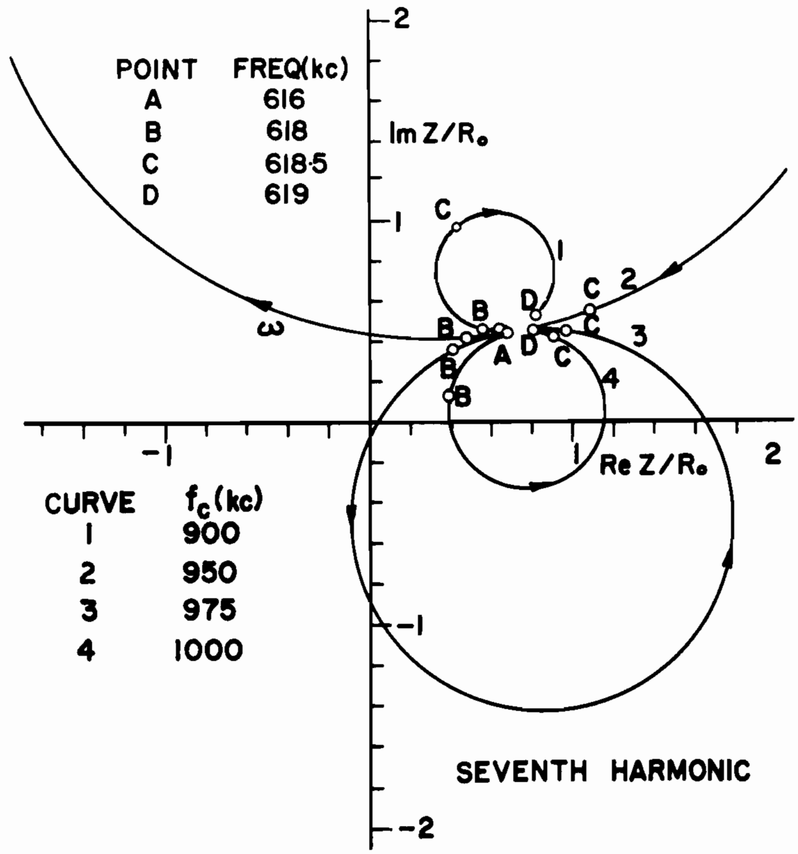

FIGURE 4.10 Seventh harmonic impedance loci for $v_D = 2v_S$, three-wave calculations using Q = 0 at cathode as boundary condition. Conductivities 4.5, 4.75, 4.88 and 5.00 (megohm cm)$^{-1}$ for curves 1, 2, 3, and 4 respectively.

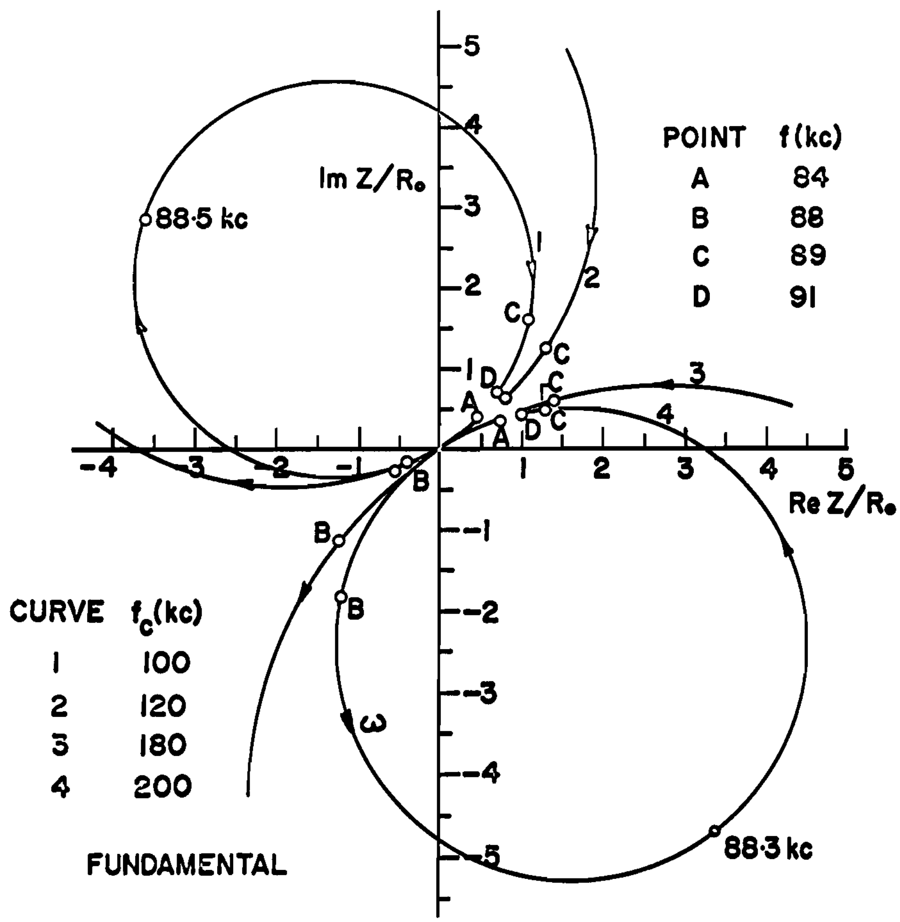

FIGURE 4.11 Fundamental impedance loci for $v_D = 2v_S$, two-wave results. Conductivities are 0.5, 0.6, 0.9 and 1.0 $(\text{megohm cm})^{-1}$ for curves 1, 2, 3 and 4 respectively.

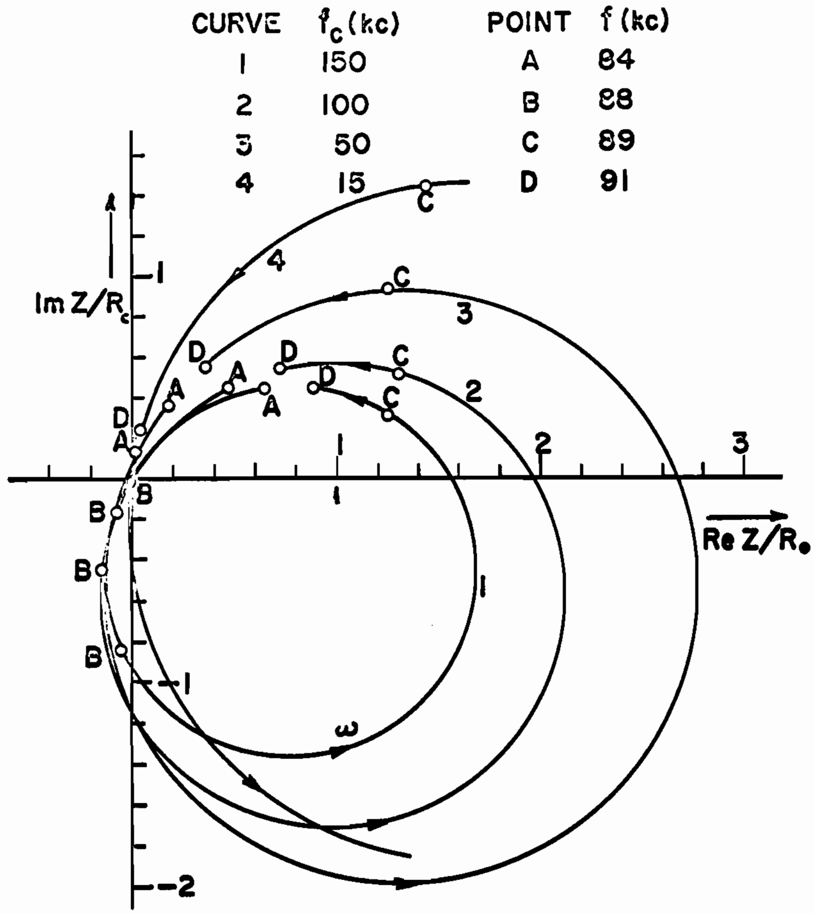

FIGURE 4.12 Fundamental impedance loci for $v_D = 2v_S$, three-wave results using D = 0 at cathode as boundary condition. Conductivities are 0.75, 0.5, 0.25 and 0.075 $(\text{megohm cm})^{-1}$ for curves 1, 2, 3 and 4 respectively.

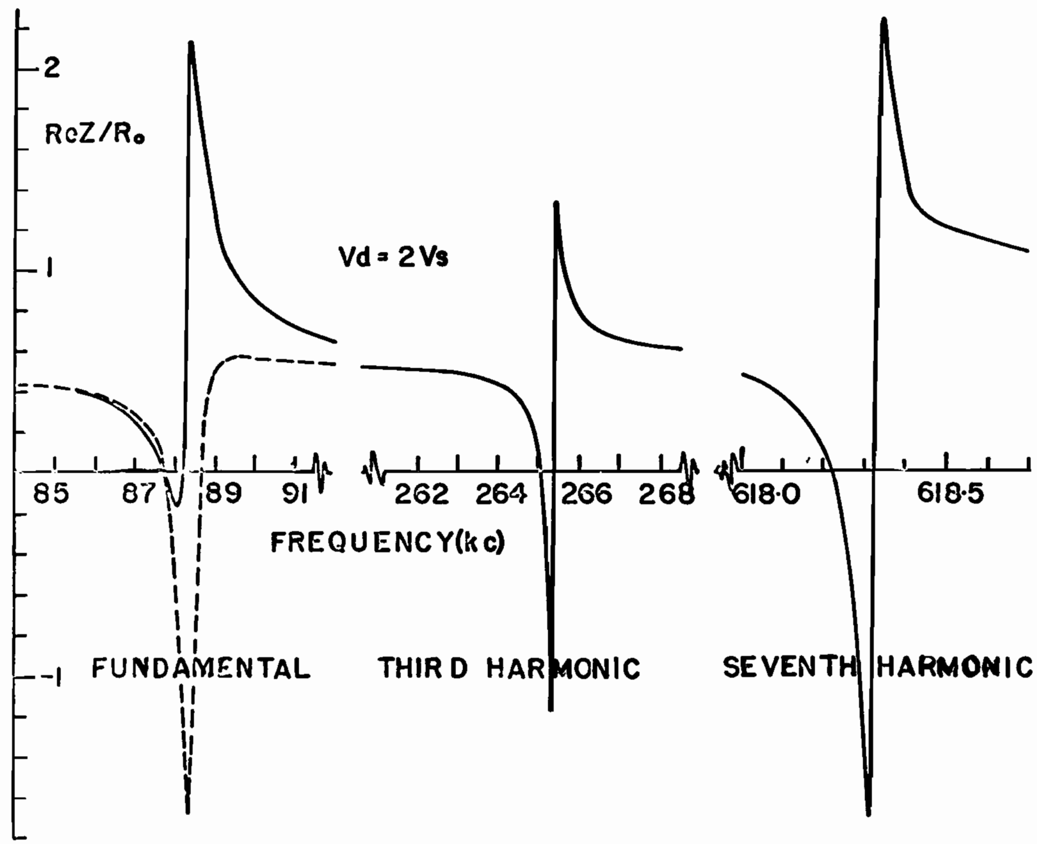

FIGURE 4.13 Real part of input impedance, three-wave results for fundamental, third harmonic and seventh harmonic. Conductivities 0.5, 1.5 and 4.75 $(\text{megohm cm})^{-1}$ respectively. Broken curve is ImZ/R_o.

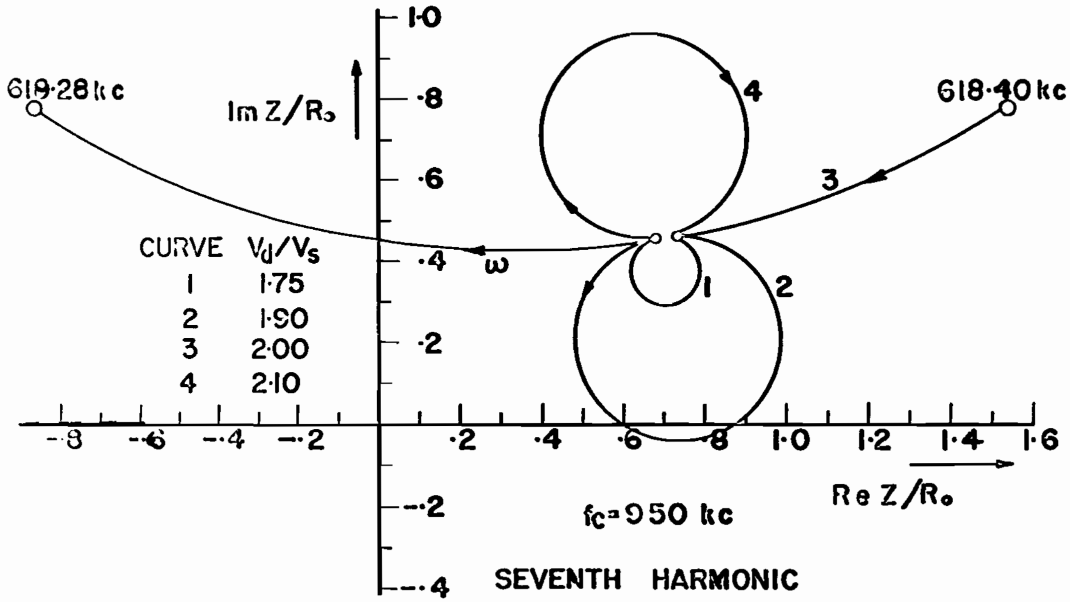

FIGURE 4.14 Seventh harmonic loci for different drift velocities for a conductivity of 4.75 (megohm cm)$^{-1}$ three-wave calculation. All curves start at 616 kc and end at 619 kc.

calculations, Figure 4.15 shows the behaviour at 100 mc which corresponds to harmonic numbers in excess of one thousand. The impedance variations are oscillatory and there is a considerable amount of negative resistance over a bandwidth which is almost equal to the fundamental frequency. The impedance loci at 100 mc, Figure 4.17, are again circles.

As an extreme case, still considering only electronic damping, calculation at 1 Gc yields the results of Figure 4.16 for a 1 mm bar and a drift velocity which is three times the velocity of sound. The negative resistance is again quite marked but the loci are no longer circular, the latter being attributed to diffusion effects.

To summarize, it seems apparent that the mechanism of acoustic amplification gives rise to a negative resistance near the mechanical resonant frequencies of the bar. This negative resistance exists up to gigacycle frequencies for appropriate choices of drift velocity and conductivity. The conductivity window over which there is negative resistance is very narrow at the low harmonic numbers and similarly the tolerance on drift velocity is small. The narrow conductivity window is characteristic of experimental results obtained under conditions of weak illumination but the conductivity values are appreciably different from those obtained experimentally.

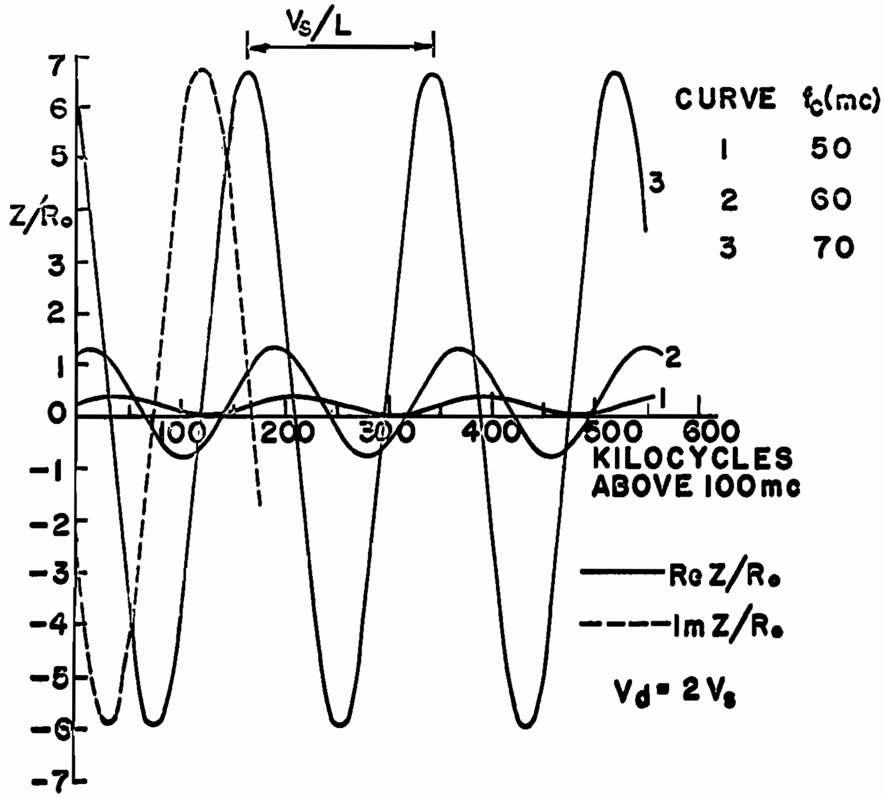

FIGURE 4.15 Real part of input impedance at 100 mc showing the negative resistance periodicity. Conductivities 0.25, 0.30 and 0.35 (kilohm cm)$^{-1}$ for curves 1, 2 and 3 respectively.

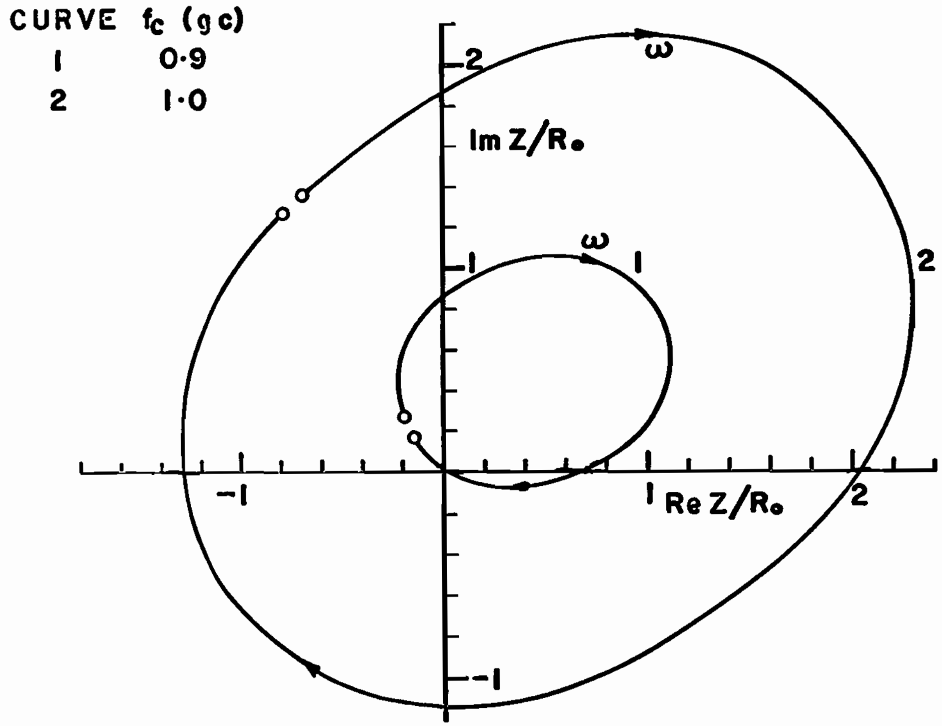

FIGURE 4.16 Impedance loci at 1000 mc for $v_D = 3v_S$, and L = 1 mm. Both curves start at 1000 mc and terminate 1.75 mc higher. Conductivities 4.5 and 5.0 $(\text{kilohm cm})^{-1}$ for curves 1 and 2.

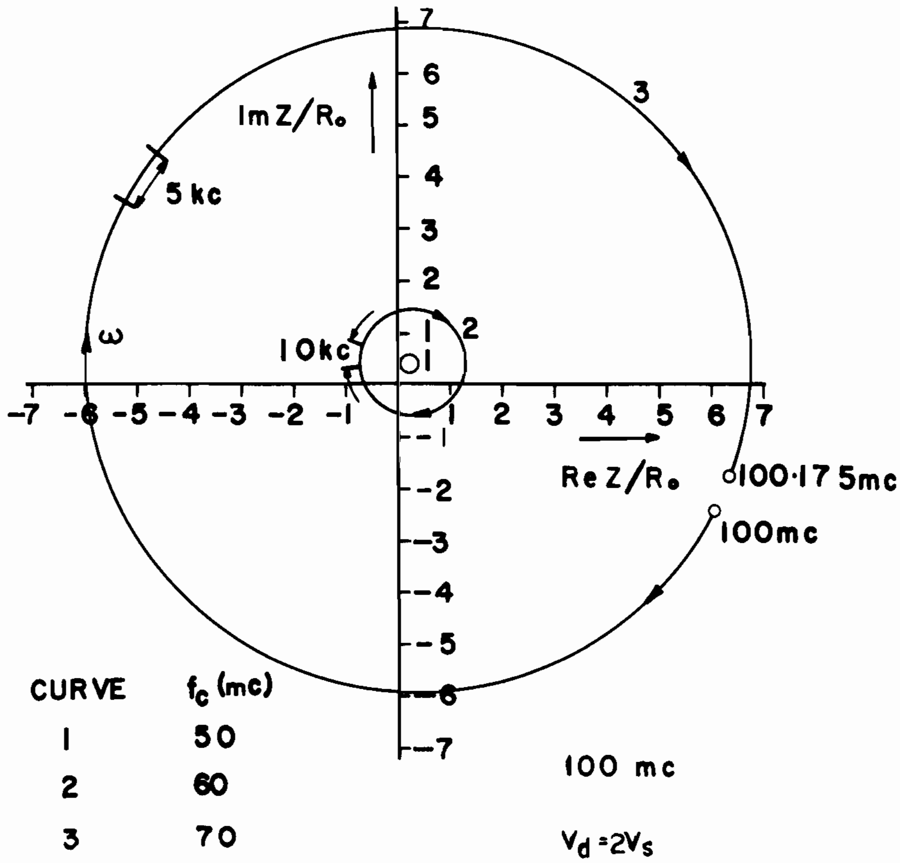

FIGURE 4.17 Same conditions as Figure 4.5 for one cycle of variation.

The above calculation is a useful starting point for a consideration of the electrical impedance of biased piezoelectric semiconductor bars. This analysis was first outlined by the author in December, 1965 at the IEEE Symposium on Sonics and Ultrasonics held at Boston, Massachusetts, in a paper entitled, "The Effect of Acoustic Gain on the Electrical Impedance of a CdS Bar." The succeeding paper at the session by A.R. Hutson, "Electrical Impedance of the Active Piezoelectric Semiconductor Resonator", described similar results. A more exact calculation would have to take into account the finite cross section of the bars at low harmonic numbers, the non-electronic damping at higher frequencies and the non-linear effects due to current saturation which, as has been shown above, can greatly modify the field distribution.

CHAPTER V

CONCLUSIONS

This thesis has been concerned with a study of acousto-electric interactions in CdS. Current oscillations were discovered during the course of research of a type which had not been previously reported. The frequency of these oscillations was very stable and occurred very close to the mechanical half-wavelength frequency of the sample bars. These results led to the detailed study of the electrical impedance of CdS bars under acoustic amplification conditions which is the principal contribution of this work. The suggestion that a negative resistance could result from acoustic gain was first made by the author. Calculations based on the impedance analysis showed such negative resistance effects at the same frequency as the measured oscillations and odd harmonic multiples. Oscillations at high harmonic numbers have been recently reported[25] the device applications of this effect are extensive.

In addition the following general conclusions are made:

1) The non-uniform field distributions observed in amplifying CdS can be quantitatively discussed in terms of

an acoustoelectric power density which is a consequence of the amplification mechanism. Current saturation occurred whenever net power went into this process. The details of the field distributions were determined by non-uniformities in conductivity.

2) The oscillations measured with non-uniform illumination were probably caused by instabilities in the high field regions favoured by gross non-uniformities in conductivity.

3) Taking trapping into account, good agreement between theory and measured performance of acoustic amplifiers was obtained.

4) Criteria have been developed for making and evaluating ohmic contacts.

As an extension of the above work it is proposed that an experimental study of the dynamics of acoustic flux growth be undertaken. This should provide information on factors determining the detailed structure of field non-uniformities and causing high field instabilities. The effect of nonlinearities on the negative resistance oscillations should be studied to ascertain the mechanism of mode selection in these oscillations.

In summary, much of the background needed for the development of a working device has been obtained, and this aspect rather than the study of new physical phenomena has been stressed in this thesis.

BIBLIOGRAPHY

1. A.R. Hutson, J.H. McFee, and D.L. White, "Ultrasonic amplification in CdS," Phys. Rev., vol. 1, p. 237, September 1961.

2. D.L. White, "Amplification of ultrasonic waves in piezoelectric semiconductors," J. Appl. Phys., vol. 33, p. 2547, August 1962.

3. A.R. Hutson and D.L. White, "Elastic wave propagation in piezoelectric semiconductors," J. Appl. Phys., vol. 33, p. 40, January 1962.

4. R.W. Smith, "Current saturation in piezoelectric semiconductors," Phys. Rev. Letters, vol. 9, p. 87, August 1962.

5. F.S. Hickernell and N.G. Sakiotis, "An electroacoustic amplifier with net electrical gain," Proc. IEEE (Correspondence), vol. 52, no. 2, pp. 194-195, February 1964.

6. J.H. McFee, "Ultrasonic amplification and nonohmic behaviour in CdS and ZnO," J. Appl. Phys., vol. 34, no. 5, pp. 1548-1553, May 1963.

7. K. Blötekjaer and C.F. Quate, "The coupled modes of acoustic waves and drifting carriers in piezoelectric crystals," Proc. IEEE, vol. 52, pp. 360-377, April, 1964.

8. I. Uchida, T. Ishiguro, Y. Sasaki, and T. Suzuki, "Effect of trapping of free carriers in CdS ultrasonic amplifier," J. Phys. Soc. (Japan), vol. 19, p. 674, May 1964.

9. H. Kroger, E.W. Prohofsky, and H.R. Carleton, "Current oscillations and collective waves in CdS," Phys. Rev. Letters, vol. 12, p. 555, May 1964.

10. H.J. McSkimin, "Measurement of ultrasonic wave velocities for solids in the frequency range 100 to 500 mc," J. Acoust. Soc. Am., vol. 34, pp. 404-409, April 1962.

11. H. Murakami, M. Miya, S. Nagano, T. Ishiguro, and I. Uchida, "Current oscillations in CdS single crystal induced by local irradiation of light," J. Appl. Phys., (Japan), vol. 3, pp. 299-300, 1964.

12. J. Okada and H. Machino, "Oscillations in Cadmium Sulfide," J. Appl. Phys., (Japan), vol. 2, pp. 736-737, 1963.

13. O. Longva, "Acoustic resonance in piezoelectric crystals," Sci. Rept. 9, Contract AF 61(052)484, Norwegian Defence Research Establishment, Norway, p. 28, March 1964.

14. E.L. Adler and G.W. Farnell, "Current oscillations and negative resistance in CdS," Proc. IEEE (Correspondence), vol. 53, p. 483, May 1965.

15. H.E. Bömmel and K. Dransfeld, "Excitation and attenuation of hypersonic waves in quartz," Phys. Rev., vol. 117, pp. 1245-1252, March 1960.

16. W.C. Wang, "Current oscillations and acoustic flux generation in CdS," Appl. Phys. Letters, vol. 6, p. 85, March 1965.

17. J.D. Maines, "Measurement of the spatial variation of electric field in amplifying CdS using the electrooptic effect," Appl. Phys. Letters, vol. 8, p. 67, February 1966.

18. H.D. Nine, "Photosensitive ultrasonic attenuation in CdS," Phys. Rev. Letters, vol. 4, p. 359, 1960.

19. E. Harnik and T. Yasar, "Structure-sensitive dependence of the attenuation characteristics of ultrasonic waves in photoconducting Cadmium Sulfide on the wavelength of illumination," J. Appl. Phys. Comm., vol. 35, p. 2086, 1964.

20. L.G. Merkulov, "Absorption of ultrasonic waves in alkali-haloid crystals," Akust. Z., vol. 5, pp. 439-445, 1959.

21. C. Kittel, "Introduction to Solid State Physics," New York: John Wiley and Sons Inc., 2nd ed., 1953, p. 515.

22. L. Clark and J. Woods, "A method of applying ohmic contacts to CdS crystals for Hall measurements," J. Sci. Instrum., vol. 42, p. 51, January 1965.

23. R. Truell, C. Elbaum, and A. Granato, "Ultrasonic attenuation in CdS above room temperature," J. Appl. Phys., vol. 35, pp. 1483-1485, May 1964.

24. C.A.A.J. Greebe, "On the frequency-dependence of the acoustoelectric effect in piezoelectric semiconductors," Phys. Letters, vol. 4, no. 1, p. 45, March 1963.

25. D.L. White, E.T. Handelman, and J.T. Hanlon, "Ultrasonic amplification in sulphur doped CdS," Proc. IEEE (Correspondence), vol. 53, p. 2157, December 1965.

26. A.R. Hutson, "Acoustoelectric explanation of non-ohmic behaviour in piezoelectric semiconductors and bismuth," Phys. Rev. Letters, vol. 9, p. 296, 1962.

27. J.E. May, "Electronic signal amplification in the UHF range with ultrasonic traveling wave amplifier," Proc. IEEE, vol. 53, pp. 1465-1485, October 1965.

28. A. Ishida, C. Hamaguchi, and Y. Inuishi, "Current saturation associated with ultrasonic amplification in CdS crystals," J. Phys. Soc. (Japan), vol. 20, pp. 1946-1956, October 1965.

29. H. Kroger, E.W. Prohofsky, and R.W. Damon, "Anomalous sound propagation in CdS," Phys. Rev. Letters, vol. 11, p. 246, September 1963.

30. J.H. McFee, private communication.

31. B.K. Ridley, "Specific negative resistance in solids," Proc. Phys. Soc. (London), vol. 82, pp. 954-966, December 1963.

32. A. Ishida, C. Hamaguchi, and Y. Inuishi, "Potential probe measurements along current-oscillating CdS crystals," J. Phys. Soc. (Japan), vol. 21, p. 186, 1966.

33. M.K. Parsons, "Note on the classical, small signal theory of acoustic-electric interaction," Proc. IEEE (Correspondence), vol. 53, p. 663, 1965.

34. G. Weinreich, "Acoustodynamic effects in semiconductors," Phys. Rev., vol. 104, pp. 321-324, October 1956.